

AD-777 259

MEASUREMENTS OF THE TEMPORAL POWER  
SPECTRA OF A PROPAGATED 10.6 MICRON  
WAVEFRONT

August J. Huber

Rome Air Development Center

Prepared for:

Advanced Research Projects Agency

February 1974

DISTRIBUTED BY:

**NTIS**

National Technical Information Service  
U. S. DEPARTMENT OF COMMERCE  
5285 Port Royal Road, Springfield Va. 22151

20. Cont'd

temporal power spectral density for the optical phase difference at the receiver.

Comparisons of the experimental data and theoretical phase difference power spectral density graphs show that several theoretical models accurately describe the spectrum at higher frequencies. A model proposed by Greenwood and based upon the work by Collins which used a von Karman spatial spectrum for the atmospheric refractive index fields is shown to be in agreement with the data at both high and low frequencies. The low-frequency spectral region was shown to be extremely sensitive to wind direction fluctuations as Collins' theory suggests.

The experimental power spectral density curves are accurately calibrated in absolute units to provide usable data for designers of optical systems whose error analysis must include the direct or indirect phase coherence degradation effects of the atmosphere.

UNCLASSIFIED

SECURITY CLASSIFICATION OF THIS PAGE (When Data Entered)

REPORT DOCUMENTATION PAGE		READ INSTRUCTIONS BEFORE COMPLETING FORM
1. REPORT NUMBER RADC-TR-74-44	2. GOVT ACCESSION NO.	3. RECIPIENT'S CATALOG NUMBER AD 777 259
4. TITLE (and Subtitle) MEASUREMENTS OF THE TEMPORAL POWER SPECTRA OF A PROPAGATED 10.6 MICRON WAVELFRONT		5. TYPE OF REPORT & PERIOD COVERED In-house Report 1 Nov 71 - 31 Oct 73
		6. PERFORMING ORG. REPORT NUMBER N/A
7. AUTHOR(s) August J. Huber		8. CONTRACT OR GRANT NUMBER(s) N/A
9. PERFORMING ORGANIZATION NAME AND ADDRESS Rome Air Development Center (OCSE) Griffiss Air Force Base, New York 13441		10. PROGRAM ELEMENT, PROJECT, TASK AREA & WORK UNIT NUMBERS 62301E, 1279, 02 01
11. CONTROLLING OFFICE NAME AND ADDRESS Rome Air Development Center (OCSE) Griffiss Air Force Base, New York 13441		12. REPORT DATE February 1974
		13. NUMBER OF PAGES 91
14. MONITORING AGENCY NAME & ADDRESS (if different from Controlling Office) Same		15. SECURITY CLASS. (of this report) Unclassified
		15a. DECLASSIFICATION DOWNGRADING SCHEDULE N/A
16. DISTRIBUTION STATEMENT (of this Report) Approved for public release; distribution unlimited.		
17. DISTRIBUTION STATEMENT (of the abstract entered in Block 20, if different from Report) Same		
18. SUPPLEMENTARY NOTES ARPA Order No. 1279 LABORATORY DIRECTORS' FUND No. DA-70-7		
19. KEY WORDS (Continue on reverse side if necessary and identify by block number) Wave Propagation Turbulent Atmosphere, Air Laser Beam Optics, Atmospheric Reproduced by NATIONAL TECHNICAL INFORMATION SERVICE U S Department of Commerce Springfield VA 22151		
20. ABSTRACT (Continue on reverse side if necessary and identify by block number) The objective of this report is to present both the experimental procedures employed and the data obtained from measurements of the temporal power spectral density of the phase coherence of an atmospherically degraded 10.6 micron wavelength laser beam. The phase coherence of the received beam was experimentally determined by use of an optical interferometer which measured the phase difference between two sampling apertures. The time history of the observed phase difference was computer processed to yield statistical estimates of the		

DD FORM 1473 1 JAN 73 EDITION OF 1 NOV 65 IS OBSOLETE

UNCLASSIFIED

SECURITY CLASSIFICATION OF THIS PAGE (When Data Entered)

MEASUREMENTS OF THE TEMPORAL POWER SPECTRA  
OF A PROPAGATED 10.6 MICRON WAVEFRONT

August J. Huber

Approved for public release;  
distribution unlimited.

LABCRATORY DIRECTORS' FUND No. DA-70-7

Do not return this copy. Retain or destroy.

10

PREFACE

The material presented in this report has been developed from the past several years efforts of the Environmental Studies Section of Rome Air Development Center. The work was funded by Laboratory Directors' Funds and by Advanced Research Project Agency Order Number 1279. The majority of this report was accepted as partial fulfillment of the requirements of a Master of Science degree in Electrical Engineering at Syracuse University.

I would like to thank Dr. Harry Gruenberg for his valuable suggestions and his careful consultation and guidance. Also, I wish to thank Raymond Urtz, Dr. Darryl Greenwood, Ronald Gleba, Donald Tarazano, and William Dungey of the Environmental Studies Section for their assistance, encouragement, and guidance in conducting the experiment.

We also appreciate the assistance of the Boundary Layer Branch of Air Force Cambridge Research Laboratory in establishing the micrometeorology program which supports these optical measurements. Their computer programs and direction in making the measurements were invaluable.

This report has been reviewed by the Office of Information, RADC, and approved for release to the National Technical Information Service (NTIS).

This report has been reviewed and is approved.

APPROVED: *Moses A. Diab*

MOSES A. DIAB  
Assistant Chief  
Space Surveillance and Instrumentation Branch

APPROVED: *William T. Pope*

WILLIAM T. POPE  
Assistant Chief  
Surveillance and Control Division

FOR THE COMMANDER: *Carlo P. Crocetti*

CARLO P. CROCETTI  
Chief, Plans Office

TABLE OF CONTENTS

CHAPTER 1 INTRODUCTION.....1

CHAPTER 2 THEORETICAL BACKGROUND.....3

    2.1 Introduction.....3

    2.2 Theoretical Phase Difference Power Spectra.....5

CHAPTER 3 DESCRIPTION OF EXPERIMENT.....23

    3.1 Introduction.....23

    3.2 Optical Measurements.....23

    3.3 Optical Receiver.....24

    3.4 Phase Measurement Technique.....26

    3.5 Meteorological Measurements.....36

    3.6 Data Recording and Reproduction.....36

CHAPTER 4 ANALYSIS OF EXPERIMENTAL DATA.....38

    4.1 Introduction.....38

    4.2 Optical Data Analysis.....38

    4.3 Meteorological Data Analysis.....46

CHAPTER 5 EXPERIMENTAL DATA.....48

    5.1 Introduction.....48

    5.2 Experimental Data.....48

CHAPTER 6 CONCLUSION.....69

    APPENDIX A.....72

TABLE OF CONTENTS (Continued)

APPENDIX B.....	78
REFERENCES.....	83

## LIST OF ILLUSTRATIONS

FIGURE 2.1	The Theoretical Phase Difference Power Spectrum Derived by Clifford.....	7
FIGURE 2.2	The Theoretical Phase Difference Power Spectrum Derived by Collins for an Orientation Angle of Zero Degrees.....	9
FIGURE 2.3	Illustration of the Orientation Angle Geometry for Theory Derived by Collins.....	10
FIGURE 2.4	The Theoretical Phase Difference Power Spectrum Derived by Collins for a Non-Zero Orientation Angle.....	12
FIGURE 2.5	The Theoretical Phase Difference Power Spectrum Derived by Greenwood as a Function of Wind Speed.....	15
FIGURE 2.6	The Theoretical Phase Difference Power Spectrum Derived by Greenwood as a Function of Orientation Angle Variance and for an Outer Scale of 2.0 m.....	16
FIGURE 2.7	The Theoretical Phase Difference Power Spectrum Derived by Greenwood as a Function of Orientation Angle Variance and for an Outer Scale of 1.0 m.....	17
FIGURE 2.8	The Theoretical Phase Difference Power Spectrum Derived by Greenwood as a Function of Outer Scale.....	18
FIGURE 2.9	Illustration of the Orientation Angle Geometry for Theory Derived by Greenwood.....	21
FIGURE 3.1	Schematic Diagram of the Optical Analyzer.....	25
FIGURE 3.2	Illustration of the Optical Reticle and the Image Plane Intensity Distribution Pattern.....	28
FIGURE 3.3	Schematic Diagram of the Digital Phase Difference Measurement Instrumentation.....	33
FIGURE 3.4	Schematic Diagram of the Inter-cycle Phase Difference Measurement Circuitry.....	35
FIGURE 5.1	The Set of Individual Phase Difference Spectra Measured on May 18, 1972.....	53
FIGURE 5.2	One Individual Phase Difference Spectrum and Appropriate Confidence Limits for May 18, 1972.....	54

LIST OF ILLUSTRATIONS (Continued)

FIGURE 5.3	Comparison of a Mean Experimental Phase Difference Power Spectrum and a Theoretical Spectrum for May 18, 1972 .....	55
FIGURE 5.3a	The Set of Individual Microtemperature Spectra Measured May 18, 1972 .....	56
FIGURE 5.3b	Comparison of the Mean Experimental Microtemperature Power Spectra and a Theoretical Spectrum for May 18, 1972 .....	57
FIGURE 5.4	Sketch of the Local Terrain Surrounding the Propagation Path .....	60
FIGURE 5.5	The Set of Individual Phase Difference Spectra Measured on May 25, 1972 .....	63
FIGURE 5.6	Comparison of a Mean Experimental Phase Difference Power Spectrum and a Theoretical Spectrum for May 25, 1972 .....	66
FIGURE 5.6a	The Set of Individual Microtemperature Spectra Measured May 25, 1972 .....	67
FIGURE 5.6b	Comparison of the Mean Experimental Microtemperature Power Spectra and a Theoretical Spectrum for May 25, 1972 .....	68
FIGURE A.1	Schematic Diagram of a Typical Twin Aperture Interferometer .....	73
TABLE 4.1	Table of Center Frequencies and Confidence Limits for Low Frequency Power Spectral Curves .....	44
TABLE 5.1	Table of Wind Speed Data for May 18, 1972 .....	50
TABLE 5.2	Table of Wind Direction Data for May 18, 1972 .....	52
TABLE 5.3	Table of Wind Speed Data for May 25, 1972 .....	61
TABLE 5.4	Table of Wind Direction Data for May 25, 1972 .....	62
TABLE B.1	Table of Reticle Errors .....	81

## Chapter 1

### INTRODUCTION

The turbulent nature of the atmosphere produces random fluctuations in its refractive index fields. The refractive index perturbations cause a degradation of the initial phase coherence of optical beams which propagate through the turbulent atmospheric medium. This phase coherence degradation can limit the performance of precision pointing and tracking systems and high resolution optical systems which must operate over an atmospheric propagation path. Statistical data describing the phase coherence variations induced by the atmosphere is therefore required for performance limit evaluation and error analysis for the previously described systems.

A convenient and useful measurement of the phase degradation is the measurement of the temporal fluctuations of the optical phase difference between two points located at the entrance plane of a receiver. The experimental measurements were performed by an optical interferometer which measured the phase difference between the two sampling apertures. The experiment consisted of measuring phase difference fluctuations for various propagation conditions. The phase difference data was then computer processed by fast Fourier transform techniques to yield experimental power spectral density estimates.

The characterization of the observed phase difference fluctuations in terms of their power spectral density yields information

directly applicable to design and error analysis studies for optical wavelength systems operating in the atmospheric medium. Graphs of the experimental phase difference power spectral density are compared to graphs of theoretical power spectral density functions derived from statistical models of the atmospheric refractive index fields. A recently proposed model which agrees with the experimental spectral data at all frequencies is described.

As an important backup to the phase measurements, microtemperature spectra were measured during the course of optical missions. Temperature fluctuations govern refractive-index fluctuations in the visible to middle infrared wavelengths. Thus, any discrepancies between theoretical and experimental phase spectra should also be seen in the microtemperature spectra. In fact, all measured spectra demonstrate more power in the low frequencies than is indicated by theory.

## Chapter 2

### THEORETICAL BACKGROUND

#### 2.1 Introduction

Optical beams propagating through the atmosphere undergo degradation of their phase and amplitude characteristics. The degradation arises from the fact that the index of refraction fields of the atmosphere are statistical random functions of their spatial and temporal coordinates. In recent years major emphasis has been placed on understanding the effect of the random refractive index fields on beam propagation for laser wavelengths. Particular attention has been paid to phase characteristics because of the coherent nature of laser light and the need to maintain coherence for a number of laser applications.

Previous experiments have been conducted to determine spatial and temporal characteristics of laser beams operating at visible wavelengths. The experiments reported here were aimed at determining the optical phase difference at two points across a spherical wave, 10.6-micron wavelength laser beam whose initial phase coherence was destroyed by propagation through the atmosphere. Theoretical expressions for the phase difference power spectrum have been derived by several investigators. The differences in these various expressions for the spectrum are due to the different assumptions used in their derivation. This section will present several theoretical expressions for the phase difference power spectrum and their most important characteristics, underlying assumptions, and differences.

Several basic assumptions about the characteristics of the refractive index fields of the atmosphere are common to all the derivations and resulting expressions. These assumptions will be explained before presenting the different expressions. Two assumptions which simplify the theory are that the atmospheric refractive index fields are three-dimensionally isotropic and homogeneous. The assumption of isotropy simplifies the three-dimensional spatial correlation functions of the refractive index field to functions of single variable scalar arguments. The assumption of statistical homogeneity of the atmospheric index fields permits writing the two-point spatial correlation functions as functions of a single variable, the separation of the two observation points. Also used for the derivation of all the following phase difference power spectrum equations is the assumption that temporal changes in the atmospheric refractive index fields at any point can be explained by use of Taylor's hypothesis.

Taylor's hypothesis proposes that the large scale mean atmospheric motions, such as those produced by wind, are the dominate transport factor for moving "frozen in" spatial variations of the refractive index field past the observation point. Through the use of this model, knowledge of the spatial statistics of the index field can be transformed to temporal statistics by use of the wind speed.

## 2.2 Theoretical Phase Difference Power Spectra

Tatarski<sup>(1)</sup> published the first derivation of an equation for the phase difference power spectrum of a light beam propagating through a turbulent atmosphere. This expression was for the special case of plane wave propagation and therefore does not directly apply to this experiment which was conducted with spherical waves.

In 1971 Clifford<sup>(2)</sup> published the theory for the spherical wave phase difference power spectrum. Clifford's resulting expression for  $W(f)$ , the phase difference power spectrum, is

$$W(f) = \begin{bmatrix} 1.0 \\ 2.0 \end{bmatrix} (.033) (2\pi\rho)^{2/3} k^2 L C_n^2 v_{\perp}^{-1} \left[ 1 - \frac{\sin X}{X} \right] X^{-2/3} \quad (2-1)$$

with the restrictions that  $f > (v_{\perp} / 2\pi L_0)$  and  $\ell_0 \ll \lambda L \ll L_0$

where  $f$  = frequency in hertz

$k = 2\pi/\lambda$ , the wavenumber of the light beam

$\lambda$  = wavelength

$L$  = propagation path length

$C_n^2$  = the optical refractive index structure constant

$\rho$  = separation of the two phase difference observation apertures

$v_{\perp}$  = wind velocity perpendicular to the propagation path

$L_0$  = size of the outer scale of turbulence

$\ell_0$  = size of the inner scale of turbulence

$X = (2\pi f \rho / v_{\perp})$

$$\begin{bmatrix} 1 \\ 2 \end{bmatrix} = \begin{matrix} 1.0 & \text{for } \rho \ll \sqrt{\lambda L} \\ 2.0 & \text{for } \rho \gg \sqrt{\lambda L} \end{matrix} .$$

Graphs of the above equation for several typical wind velocities are shown in Fig. 2.1. The curves have a  $-8/3$  power slope at higher frequencies,  $f > \sqrt{6} v_{\perp} / 2\pi\rho$ , and a  $-2/3$  slope at lower frequencies where  $v_{\perp} / 2\pi L_0 < f < \sqrt{6} v_{\perp} / 2\pi\rho$ . The curves do not extend below the frequency  $f = v_{\perp} / 2\pi L_0$  because that is the lower limit of validity of the equation.

Clifford's derivation of the phase difference power spectrum included the three previously explained suppositions of three-dimensional isotropy, statistical homogeneity, and applicability of Taylor's hypothesis for the atmospheric refractive index fields. Clifford also assumed that the vector,  $\rho$ , which connects the two phase difference observation apertures and the vector,  $v_{\perp}$ , which describes the horizontal wind velocity are coplanar in a horizontal plane and are also parallel. Implicit in Clifford's derivation is the applicability of the Kolmogorov refractive index spectrum

$$\Phi_n(K) = .033 C_n^2 K^{-1/3} \quad (2-2)$$

in which the variable  $K = 2\pi/\ell$  is the spatial frequency proportional to scale size  $\ell$ . This spectrum is valid only for refractive index perturbations of scale sizes in the range  $\ell_0 < \ell < L_0$  where  $\ell_0$  and  $L_0$  are the inner and outer scales of turbulence in the atmosphere. The use of this specific refractivity spectrum is the source of the two restrictions,  $f > v_{\perp} / 2\pi L_0$  and  $\ell_0 \ll \sqrt{\lambda L} \ll L_0$ , on Clifford's final equation.

Collins<sup>(3)</sup> has presented two different expressions for the phase difference power spectrum. The first expression extends

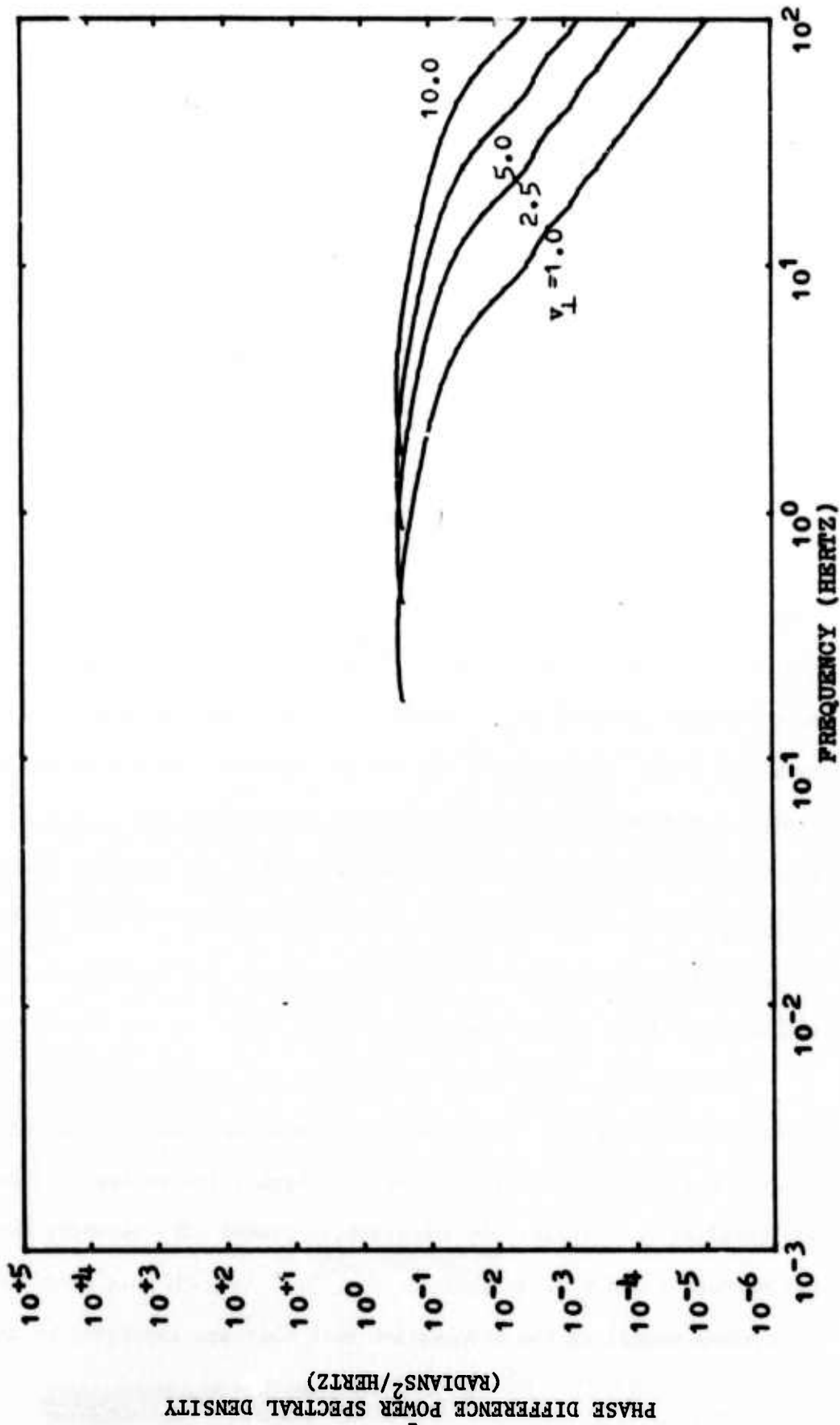


Fig. 2.1. Theoretical phase difference spectra derived by Clifford for  $p=0.125$  m,  $L_0=1.0$  m, and  $v_L=1.0, 2.5, 5.0,$  and  $10.0$  m/s.

the region of validity of Clifford's spectrum to frequencies less than  $v_{\perp}/2\pi L_0$  and is for the case where the vectors  $\rho$  and  $v_{\perp}$  are horizontally coplanar and parallel. The second expression is also valid for frequencies less than  $v_{\perp}/2\pi L_0$  but is for the case for which vectors  $\rho$  and  $v_{\perp}$  are not horizontally coplanar and parallel.

Collins' phase difference power spectrum equation for the case in which vectors  $\rho$  and  $v_{\perp}$  are horizontally coplanar and parallel is

$$W(f) = \begin{bmatrix} 1.0 \\ 2.0 \end{bmatrix} (.033)(2\pi\rho)^{3/2} k^2 LC_n^2 v_{\perp}^{-1} [X^2 + R^2]^{-4/3} \left[ 1 - \frac{\sin X}{X} \right] \quad (2-3)$$

with the restriction that  $\ell_0 \ll \sqrt{\lambda L}$  where  $R = A\rho/L_0$ ,  $A = 1.071$ , and all other quantities are as defined for (2-1). Fig. 2.2 shows this equation plotted for a variety of typical values of  $v_{\perp}$ , the mean wind speed perpendicular to the propagation path and horizontally coplanar with and parallel to vector  $\rho$ . The spectra in Fig. 2.2 are for a small observation aperture separation,  $\rho$ , and have a  $-8/3$  power dependency in the high frequency region where  $f > \sqrt{6} v_{\perp}/2\pi\rho$ , a  $-2/3$  power slope in the mid-frequency region, and a  $+2$  slope for the low frequency region where  $f < v_{\perp}/2\pi L_0$ .

Collins has also derived an equation for the phase difference power spectrum for the case in which the mean horizontal wind velocity vector,  $v_{\perp}$ , and the observation aperture separation vector,  $\rho$ , are not parallel and coplanar in a horizontal plane. The geometry for the vectors  $\rho$  and  $v_{\perp}$ , as shown in Fig. 2.3, is such that when viewed in a plane normal to the propagation path they are separated by an

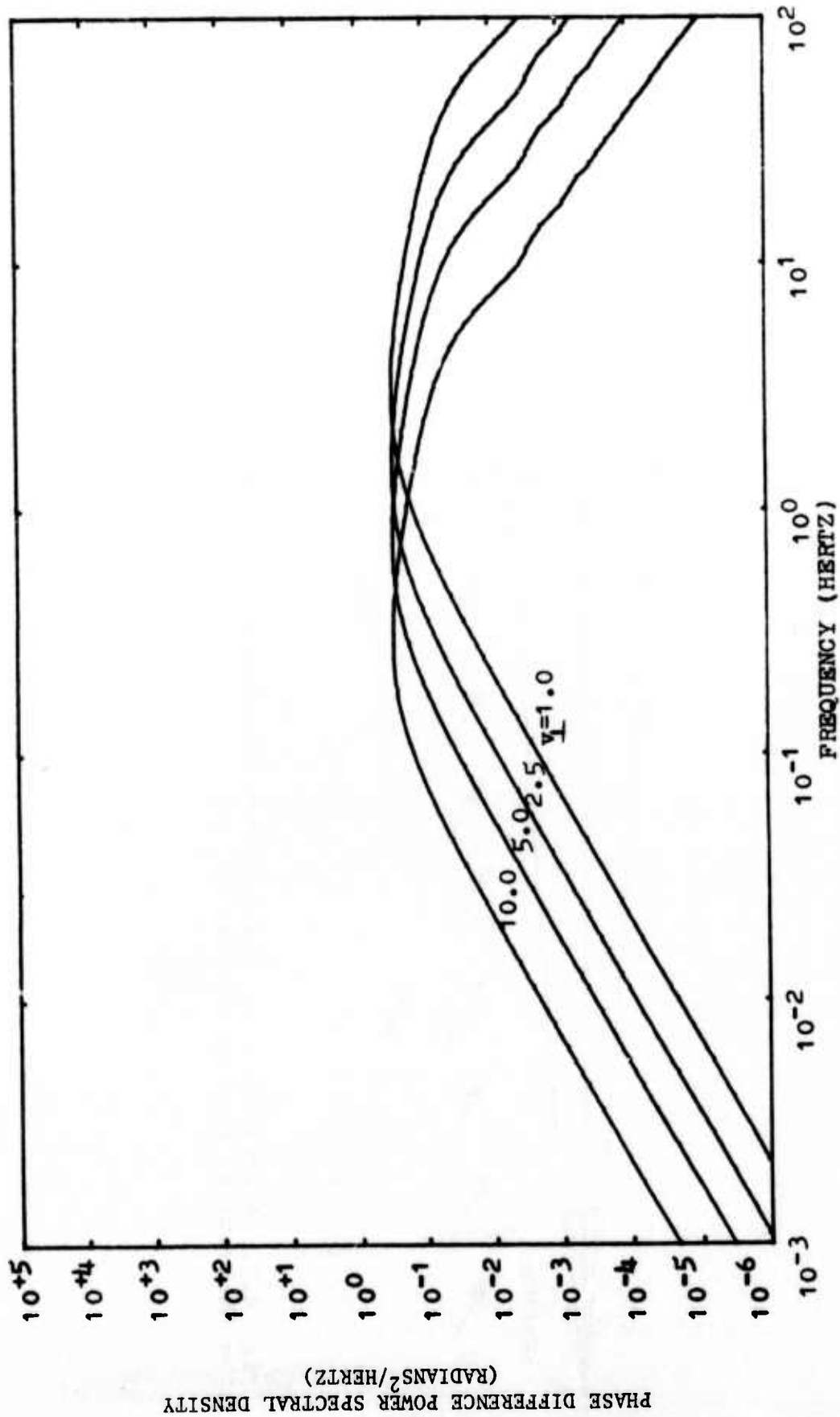


Fig. 2.2. Theoretical phase difference spectra derived by Collins for p and v co-planar and parallel,  $p=0.125$  m,  $L_0=1.0$  m, and  $v_L=1.0, 2.5, 5.0,$  and  $10.0$  m/s.

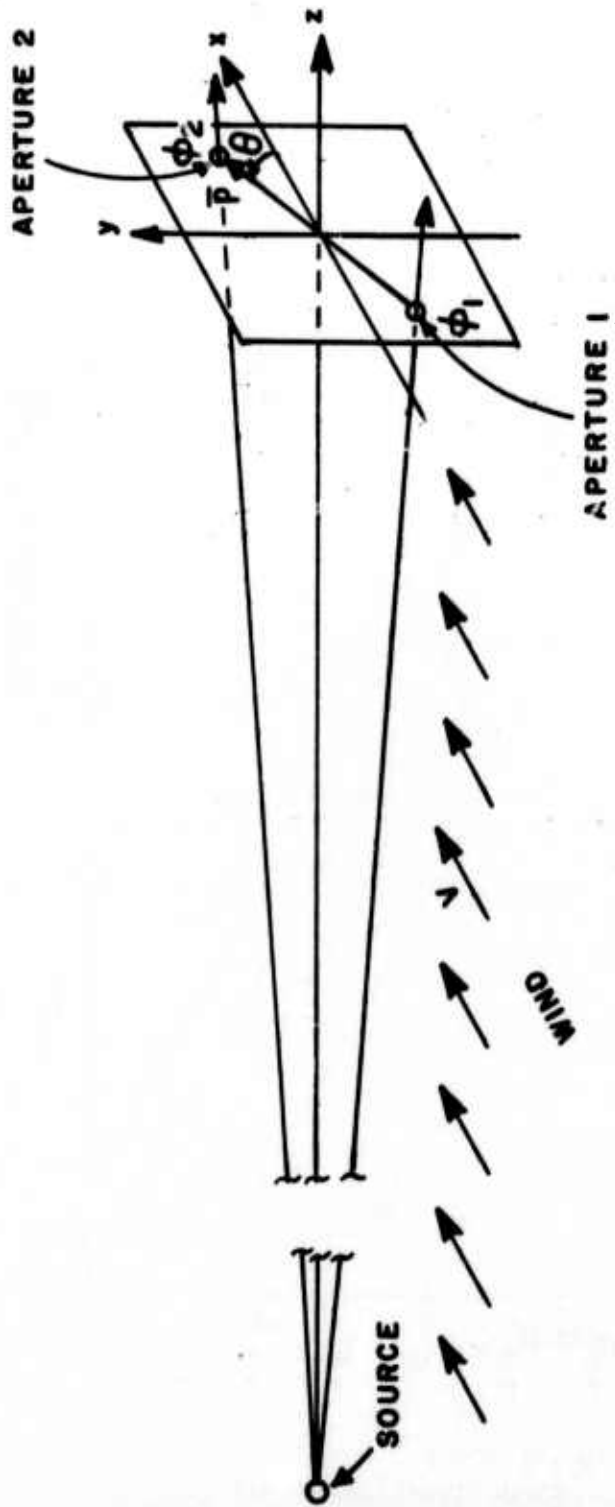


Fig. 2.3. Illustration of the geometry describing the orientation angle,  $\theta$ , for the theoretical work by Collins.

orientation angle,  $\theta$ . The resulting power spectral density equation has two general forms; the first is valid for low and mid-range frequencies and the second for high frequencies. The two forms and their regions of validity are

$$W(f) = \begin{bmatrix} 1.0 \\ 2.0 \end{bmatrix} (.033) (2\pi\rho)^{8/3} k^2 LC_n^2 v_{\perp}^{-1} [X^2 + R^2]^{-4/3} \left[ \frac{X^2 \cos^2(\theta)}{6} + \frac{(X^2 + R^2) \sin^2(\theta)}{4} \right] \quad (2-4)$$

valid for  $|X \cos(\theta) \pm (X^2 + R^2)^{1/2} \sin(\theta)| < \sqrt{6}$

and

$$W(f) = \begin{bmatrix} 1.0 \\ 2.0 \end{bmatrix} (.033) (2\pi\rho)^{8/3} k^2 LC_n^2 v_{\perp}^{-1} [X^2 + R^2]^{-4/3} \quad (2-5)$$

valid for  $|X \cos(\theta) \pm (X^2 + R^2)^{1/2} \sin(\theta)| > \sqrt{6}$ .

The above expressions properly combined to extend over both regions of validity are shown in Fig. 2.4 for small separation,  $\rho$ , the case of interest for this experiment. The high and medium frequency regions are independent of the orientation angle and exhibit the previously seen  $-8/3$  and  $-2/3$  power characteristics, respectively. However, in the low frequency region,  $f < v_{\perp} / 2\pi L_0$ , the curves flatten out at a value proportional to the quantity

$$\begin{bmatrix} 1 \\ 2 \end{bmatrix} (.033) k^2 LC_n^2 (2\pi\rho)^{8/3} v_{\perp}^{-1} (0.25 R^2 \sin^2 \theta).$$

The basic assumptions used by Collins to derive the theoretical phase difference spectra for both cases are identical. The first three suppositions, also used by Clifford, are three-dimensional isotropy, homogeneity, and the applicability of Taylor's hypothesis for the atmospheric refractive index fields. For both of Collins' derivations the Kolmogorov refractive index spectrum used by

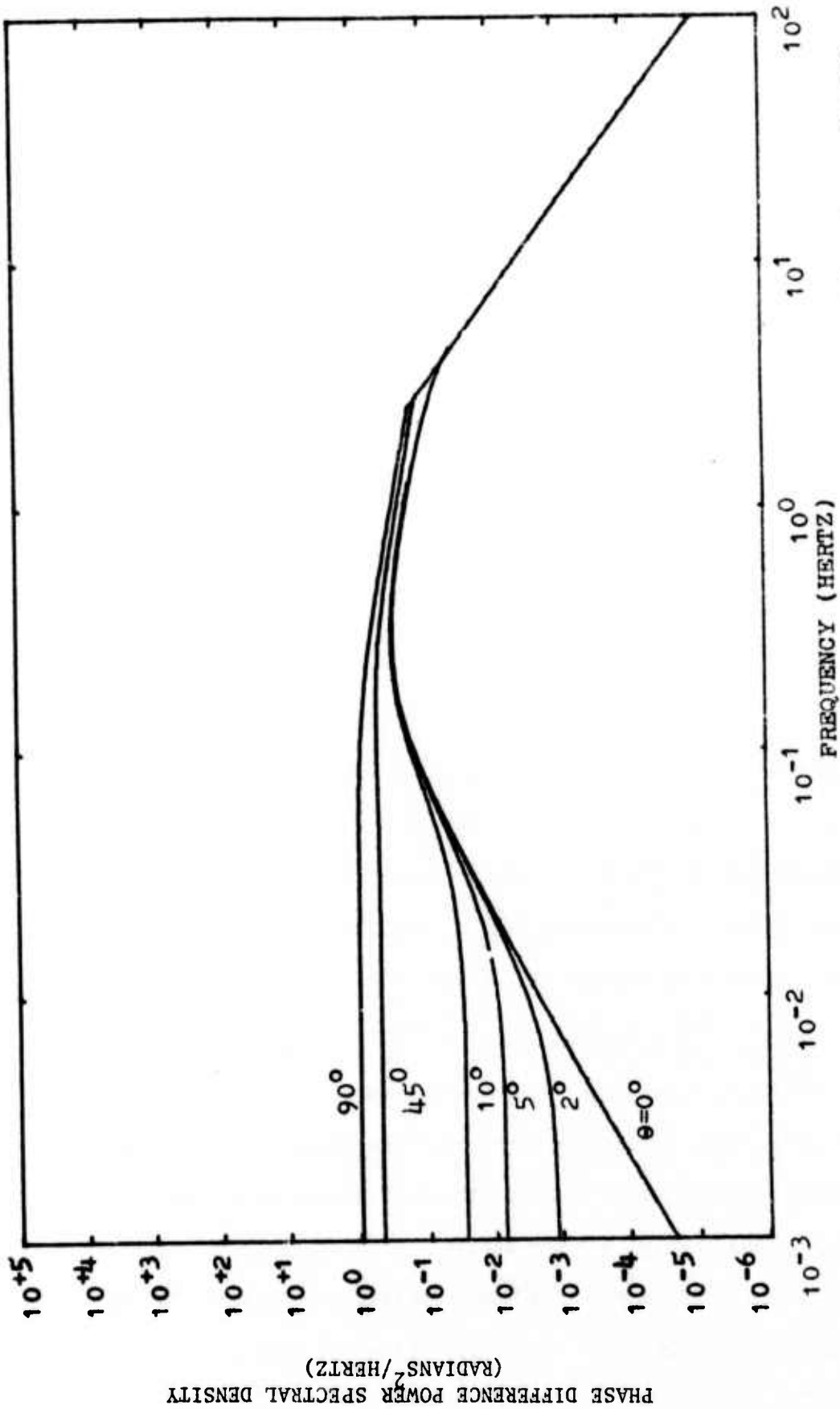


Fig. 2.4. Theoretical phase difference spectra derived by Collins for  $p=0.125$  m,  $L_0=1.0$  m,  $v_1=1.0$  m/s, and  $\theta=0^\circ, 2^\circ, 5^\circ, 10^\circ, 45^\circ$ , and  $90^\circ$ .

Clifford, was changed to the modified von Karman spectrum,

$$\phi_n(K) = (.033)C_n^2 \left[ (A/L_0)^2 + K^2 \right]^{-1/6}. \quad (2-6)$$

The parameter  $K = 2\pi/\ell$  is the refractive index spatial frequency corresponding to scale size  $\ell$ . In the spatial domain this refractivity spectrum is theoretically valid for scale sizes both within the inertial subrange of turbulence,  $\ell_0 < \ell < L_0$ , and for scale sizes larger than the outer scale of turbulence,  $\ell > L_0$ . This extension of the refractive index spatial spectrum to include scale sizes greater than the outer scale was responsible for extending the temporal phase difference spectrum to the low-frequency region defined as  $f < v_{\perp} / 2\pi L_0$ .

Greenwood<sup>(4)</sup> has performed an analysis of the phase difference power spectrum which is an extension of Collins' theory for a nonzero orientation angle. Greenwood's analysis assumes that the orientation angle,  $\theta$ , is a random variable which is dependent upon the horizontal wind direction, the vertical wind velocity variance, and the small offset angle of the observation apertures from the horizontal position. The final result is a mean phase difference power spectrum,  $\langle W(f) \rangle$ , averaged over the random variable  $\theta$ , the orientation angle. The equations for the spectrum are

$$\langle W(f) \rangle = \begin{bmatrix} 1.0 \\ 2.0 \end{bmatrix} (.033)(2\pi\rho)^{2/3} k^2 L C_n^2 v_{\perp}^{-1} \left[ X^2 + R^2 \right]^{-4/3} \left[ \frac{X^2}{6} \right] \left[ 1 + \frac{3R^2 r}{2X^2} \right] \quad (2-7)$$

valid for  $|X \cos(\theta) \pm (X^2 + R^2)^{1/2} \sin(\theta)| \ll \sqrt{6}$

and

$$\langle W(f) \rangle = \begin{bmatrix} 1.0 \\ 2.0 \end{bmatrix} (.033)(2\pi\rho)^{2/3} k^2 L C_n^2 v_{\perp}^{-1} \left[ X^2 + R^2 \right]^{-4/3} \quad (2-8)$$

valid for  $|X \cos(\theta) \pm (X^2 + R^2)^{1/2} \sin(\theta)| \gg \sqrt{6}$

where  $r = \langle \theta^2 \rangle = \langle \theta \rangle^2 + \langle \theta - \langle \theta \rangle \rangle^2$ .

The brackets indicate ensemble averages over the random variable  $\theta$ . Replacing the  $X^2/6$  term in the first expression above by

$$[1 - (\sin X)/X] \text{ results in the expression} \\ \langle W(f) \rangle = \begin{bmatrix} 1.0 \\ 2.0 \end{bmatrix} (.033) (2\pi\rho)^{8/3} k^2 L C_n^2 v_{\perp}^{-1} [X^2 + R^2]^{-4/3} \left[ 1 - \frac{\sin X}{X} \right] \left[ 1 + \frac{3R^2 r}{2X^2} \right] \quad (2-9)$$

which is a generalization of (2-3) for all frequencies.

The parameters in the above equation which have the greatest effect on the shape of the spectrum are:  $r$ , the second moment of the orientation angle;  $L_0$ , the turbulence outer scale size which determines  $R$ ; and  $v_{\perp}$ , the mean horizontal wind speed perpendicular to the propagation path. Fig. 2.5 is a graph of (2-9) for values of 1, 2.5, 5, 7.5, and 10 meters per second for parameter  $v_{\perp}$ . For larger values of  $v_{\perp}$  the shift to the right of the upper and lower frequency breakpoints of the spectrum,  $f = \sqrt{6} v_{\perp} / 2\pi\rho$  and  $f = Av_{\perp} / 2\pi L_0$ , respectively, is very clearly shown. Fig. 2.6 is a graph of the spectrum for various typical values of parameter  $r$ , for an outer scale of one meter, and for a normal mean wind speed of one meter per second. Fig. 2.7 is another graph for the same parameters as Fig. 2.6 with the exception of outer scale size which is two meters. These two preceding graphs clearly show the effect of parameter  $r$  on the shape of the spectrum at low frequencies. Fig. 2.8 shows that the effect of an increasing outer scale size on the low frequency portion of the spectrum is to lower the low frequency spectral breakpoint of  $f = Av_{\perp} / 2\pi L_0$  and raise the low frequency level of the curve.

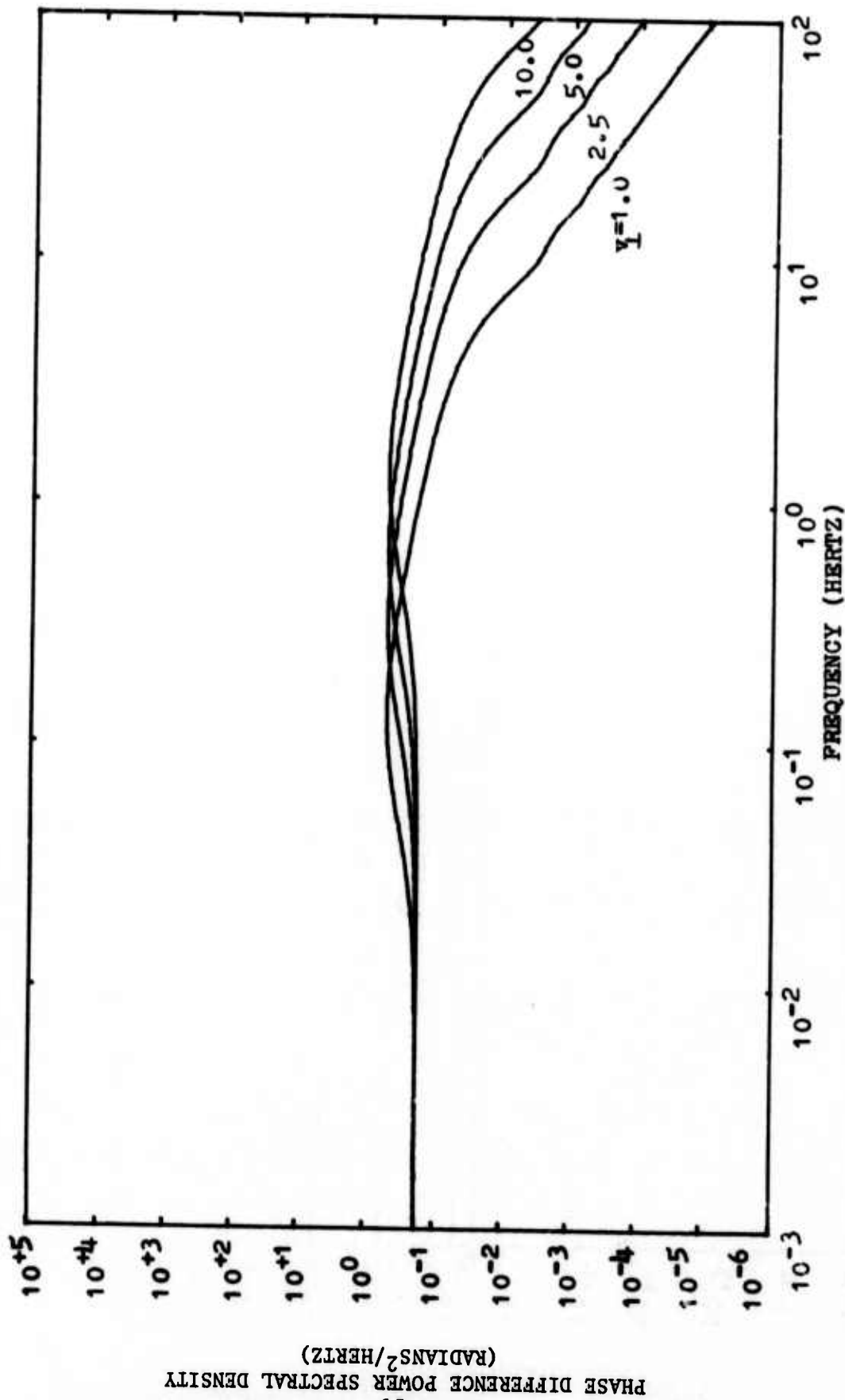


Fig. 2.5. Theoretical phase difference spectra derived by Greenwood for  $p=0.125$  m,  $L_0=2.0$  m,  $r=0.12$  rad<sup>2</sup>, and  $\gamma_1=1.0, 2.5, 5.0, 10.0$  m/s.

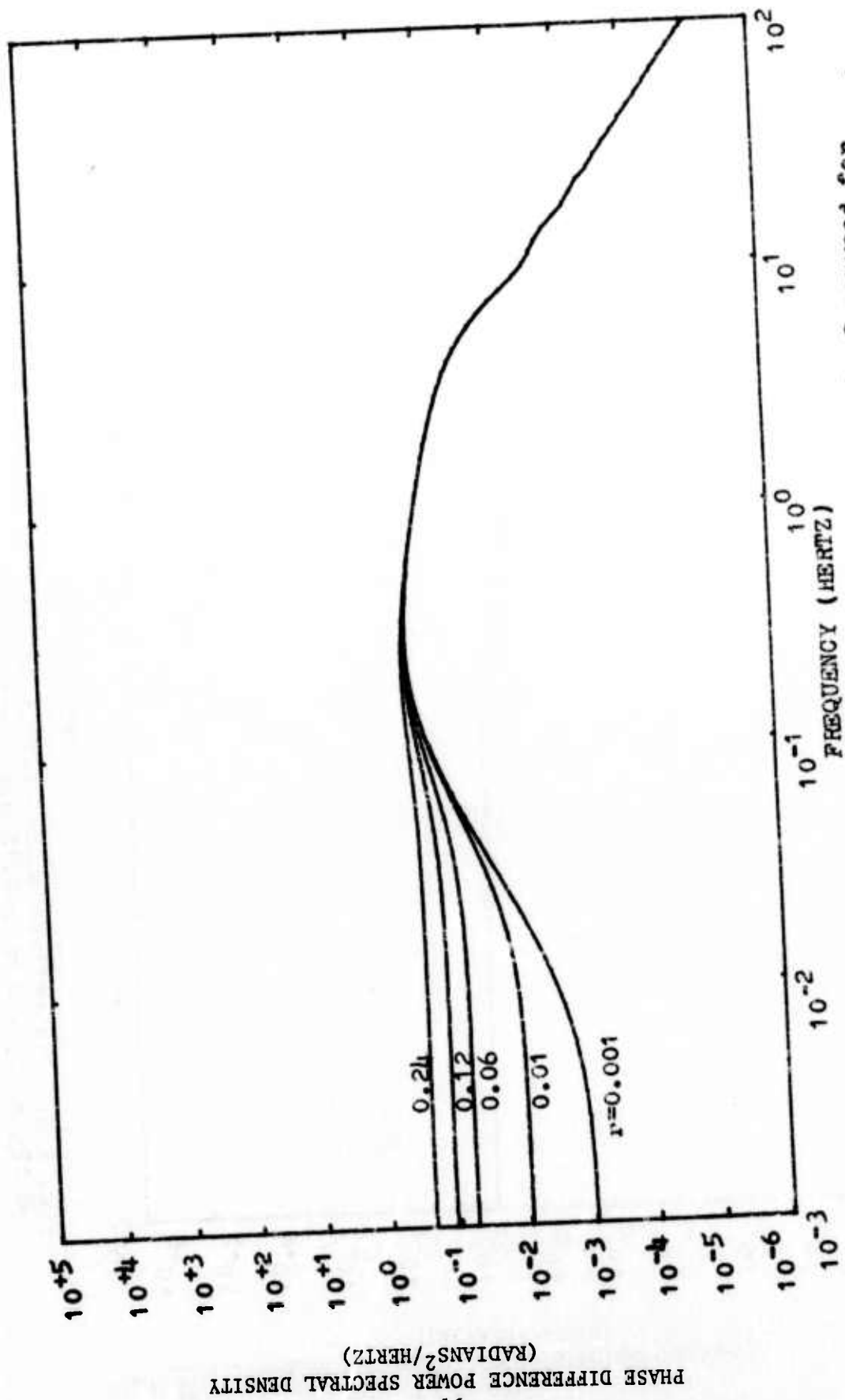


Fig. 2.6. Theoretical phase difference spectra derived by Greenwood for  $p=0.125$  m,  $L_0=1.0$  m,  $v_1=1.0$  m/s, and  $r=0.001, 0.01, 0.06, 0.12, \text{ and } 0.24$  rad<sup>2</sup>.

PHASE DIFFERENCE POWER SPECTRAL DENSITY (RADIANS<sup>2</sup>/HERTZ)

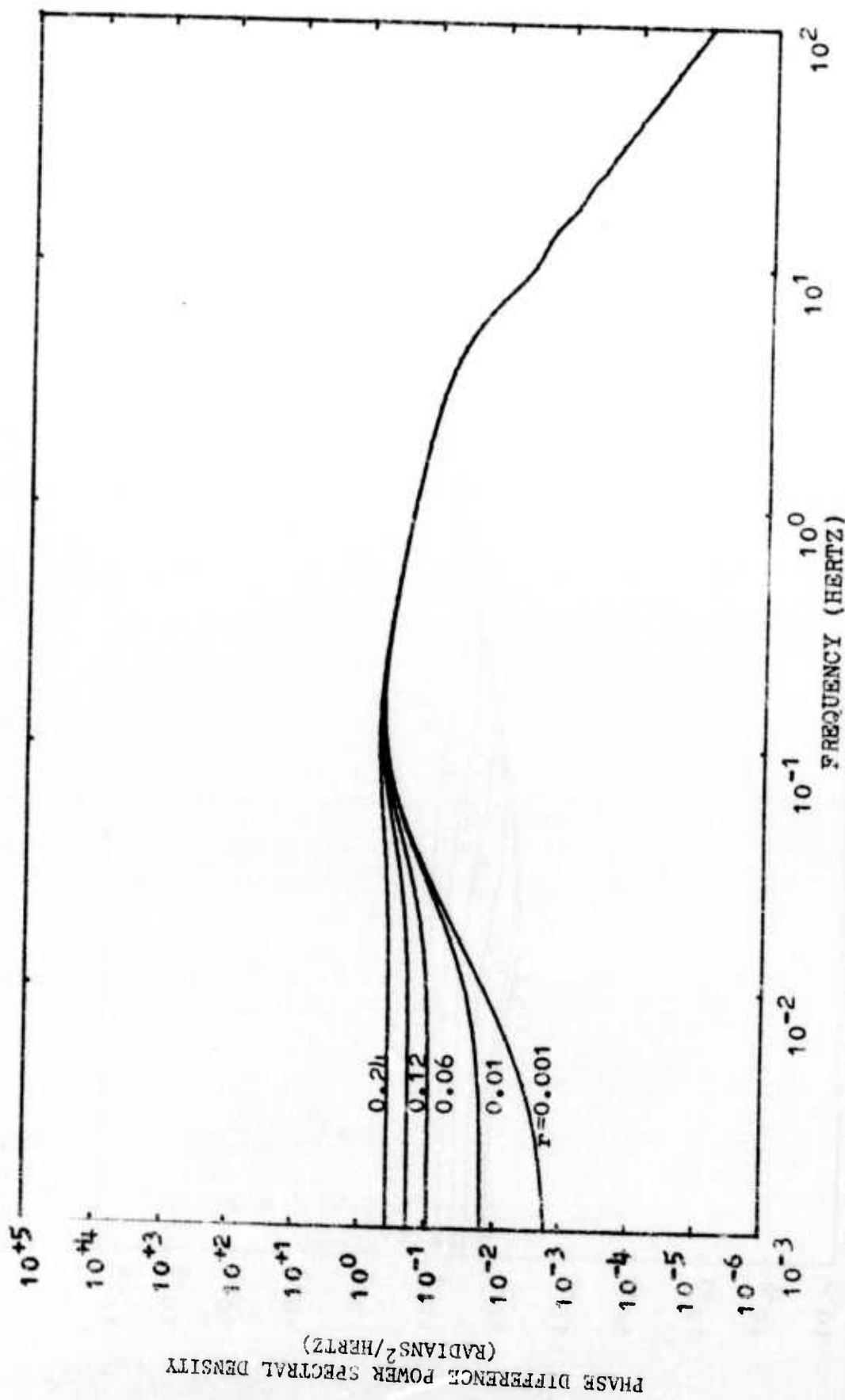


Fig. 2.7. Theoretical phase difference spectra derived by Greenwood for  $p=0.125$  m,  $L_0=2.0$  m,  $v_1=1.0$  m/s, and  $r=0.001, 0.01, 0.06, 0.12, \text{ and } 0.24$  rad<sup>2</sup>.

PHASE DIFFERENCE POWER SPECTRAL DENSITY  
(RADIAN<sup>2</sup>/HERTZ)

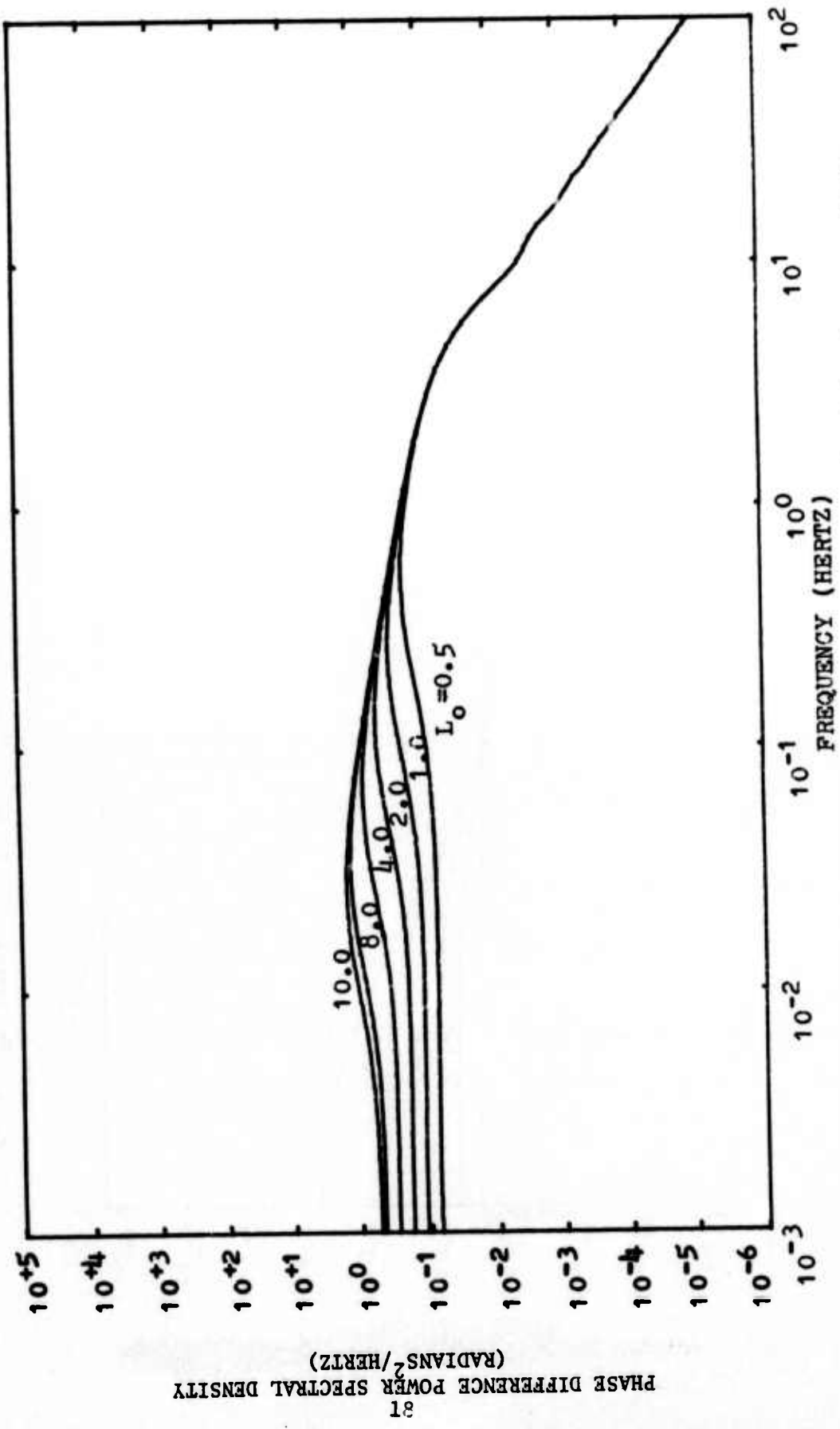


Fig. 2.8. Theoretical phase difference spectra derived by Greenwood for  $p=0.125$  m,  $v_{\perp}=1.0$  m/s,  $r=0.12$  rad<sup>2</sup>, and  $L_0=0.5, 1.0, 2.0, 4.0, 8.0,$  and  $10.0$  m.

In general the equation for the phase difference power spectrum developed by Greenwood has the  $-8/3$  and approximate  $-2/3$  slopes at high and medium frequencies as exhibited by the previous spectra derived by Clifford and Collins. However, unlike the previous curves for small orientation angles, these curves show a low-frequency flattening trend at a level within one decade of the medium frequency spectral peak. The actual level of the theoretical spectra at low frequencies is

$$\left[ \begin{array}{l} 1 \\ 2 \end{array} \right] (.033)k^2 LC_n^2 (2\pi\rho)^{3/2} v_{\perp}^{-1} (1/4)R^2.$$

As previously stated Greenwood's expression is a modification of Collins' work, equations 2-4 and 2-5, for a nonzero orientation angle,  $\theta$ . The assumptions employed by Greenwood include all those used by Collins plus several additional assumptions explained below. The orientation angle,  $\theta$ , is assumed to be a Gaussian distributed random variable, thereby simplifying the determination of mean values for  $\cos^2\theta$  and  $\sin^2\theta$  according to the equations

$$\langle \cos^2(\theta) \rangle = \frac{1}{2} \left[ 1 + e^{-2\sigma^2} \cos(2\eta) \right] \quad (2-10)$$

$$\langle \sin^2(\theta) \rangle = \frac{1}{2} \left[ 1 - e^{-2\sigma^2} \cos(2\eta) \right] \quad (2-11)$$

where  $\eta$  = the mean value of  $\theta$

$\sigma^2$  = the variance of  $\theta$ .

For this experiment we may assume that the mean value of  $\theta$  is very small and that the variance of  $\theta$  is also fairly small so that the above equations may be approximated by

$$\langle \cos^2(\theta) \rangle \approx 1 \quad (2-12)$$

$$\langle \sin^2(\theta) \rangle \approx \langle \theta^2 \rangle. \quad (2-13)$$

Fig. 2.9 shows the geometry describing the resulting situation. Restricting the solution to small values of  $\theta$  such that  $\theta \approx \tan\theta$  and assuming a small variance for the component of horizontal wind speed perpendicular to the propagation path the resulting approximation is

$$\langle \theta^2 \rangle \approx \frac{\langle v_{\text{vert}}^2 \rangle}{\langle v_{\perp} \rangle^2} \quad (2-14)$$

or

$$\langle \theta^2 \rangle \approx \frac{\langle v_{\text{vert}}^2 \rangle}{\langle V \rangle^2 \cos^2(\phi)} \quad (2-15)$$

where  $v_{\text{vert}}$  = the vertical wind speed component

$v_{\perp}$  = the horizontal wind speed component perpendicular to the propagation path

$V$  = the horizontal wind speed

$\phi$  = the angle separating  $\langle V \rangle$  and  $\langle v_{\perp} \rangle$ .

From boundary layer turbulence theory the expression for estimating the second moment of the vertical wind velocity is given as <sup>(5,6)</sup>

$$\langle v_{\text{vert}}^2 \rangle \approx 1.75 \left[ \frac{.4 \langle V \rangle}{\ln(Z/Z_0)} \right]^2 \quad (2-16)$$

or

$$\langle v_{\text{vert}}^2 \rangle \approx \frac{.28 \langle V \rangle^2}{[\ln(Z/Z_0)]^2} \quad (2-17)$$

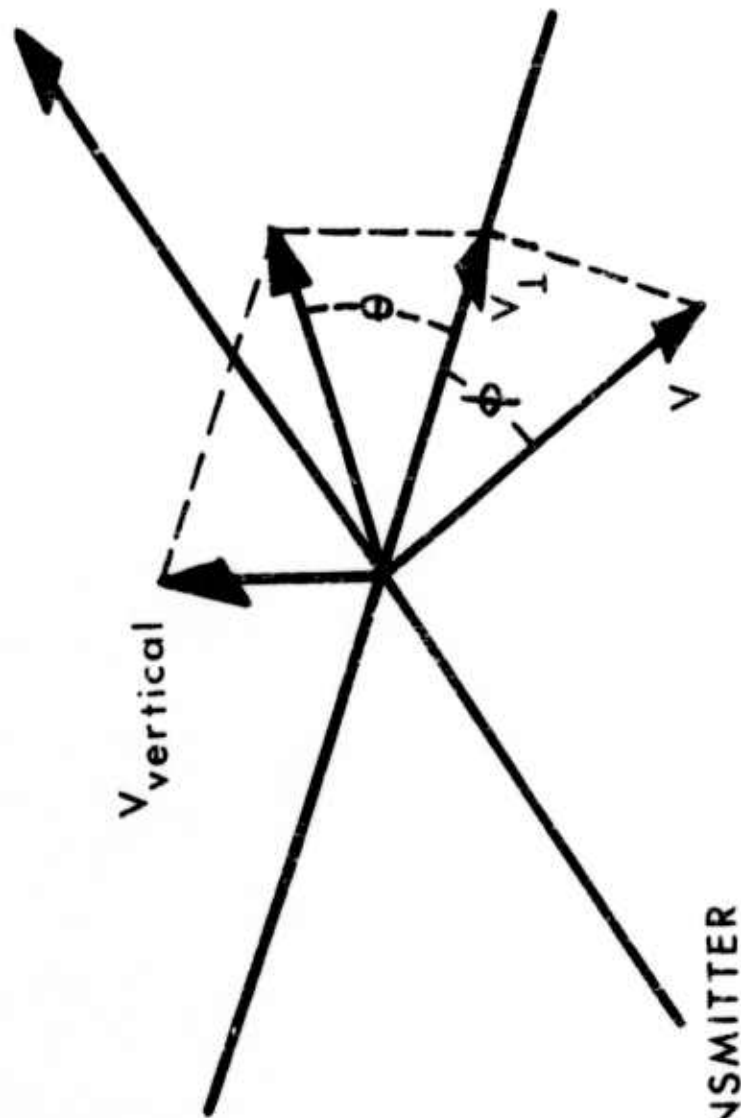
where  $Z_0$  = a surface roughness scale of approximately one to five centimeters

$Z$  = the height of the laser beam above ground.

The final approximate relationship for  $\langle \theta^2 \rangle$  is

$$\langle \theta^2 \rangle \approx .28 / [\cos(\phi) \ln(Z/Z_0)]^2. \quad (2-18)$$

RECEIVER



TRANSMITTER

Fig. 2.9. Illustration of the geometry describing the orientation angle,  $\theta$ , and the wind velocity vectors  $V_{\text{vert}}$  and  $V_1$  for Greenwood's theoretical work.

The result is that  $\langle \cos^2(\theta) \rangle \approx 1.0$  and  $\langle \sin^2(\theta) \rangle \approx \langle \theta^2 \rangle = r$  which are then used to derive (2-9).

The major restrictions arising from the above approximations and assumptions are that  $\eta$  be very small and that angle  $\phi$  be less than plus or minus 45 degrees which restricts angle  $\theta$  to fairly small values.

Greenwood's expression for the spectrum exhibits the same  $-8/3$  and  $-2/3$  power dependencies at high and medium frequencies as did the spectra derived by Clifford and Collins. In the low frequency region, however, only Greenwood's spectrum has a flattening trend for small orientation angles. This low frequency flattening trend was typical of experimental data measured under conditions of strong to medium turbulence as is shown by our experimental spectra.

## Chapter 3

### DESCRIPTION OF EXPERIMENT

#### 3.1 Introduction

Optical phase difference experiments at 10.6 micron wavelengths were conducted from February through May, 1972 at the Rome Air Development Center Verona test site. The following is a description of the simultaneous measurements that were made of optical and meteorological parameters.

#### 3.2 Optical Measurements

For the optical measurements, laser beams were propagated through the atmosphere for a distance of 300 meters over a path parallel to and one meter above the ground. The beam was propagated between the transmitter and receiver buildings in a direction  $36^\circ$  south of west over uniform, grassy, level terrain. The prevailing winds were from the northwest at an angle of  $80^\circ$  to the propagating laser beams. However, the prevailing winds were not always present on days that experiments were conducted as will be shown by the data.

The transmitter was located in a small, weather-proofed shelter and mounted on a stable concrete slab. The transmitter consisted of a 7-watt, continuous-wave, 10.6-micron wavelength carbon dioxide laser and a 50-milliwatt, Q6328-micron helium-neon laser whose beams were combined and transmitted coaxially. Before leaving the transmitter, the two beams were demagnified to approximate a spherical wave source. The helium-neon beam was used only for pointing and

directing the carbon dioxide beam into the receiver. The measurements were performed upon the carbon dioxide laser beam.

### 3.3 Optical Receiver

The optical receiver, shown schematically in Fig. 3.1, consisted of a 16-inch diameter Boller and Chivens Cassegrain telescope and an optical propagation effects analyzer built by the Perkin-Elmer Company. The telescope collected the energy of the received wavefront and focused it at the primary focus of the optical analyzer. The telescope was of astronomical quality with optics of one-tenth of a wavelength smoothness at 0.6 microns. Consequently, effects from the smoothness of the telescope surfaces were negligible for our experiments at 10.6 microns. The Perkin-Elmer optical propagation analyzer was capable of performing various optical light beam experiments. For this experiment, the analyzer was placed in a twin-aperture-interferometer configuration to measure the optical phase difference between two projected sampling aperture points on the received wavefront. For convenience in the optical analyzer block diagram, Fig. 3.1, the Cassegrain receiving telescope and the two reflective Dall-Kirkham systems are illustrated as refractive objectives. As shown in Fig. 3.1, the primary Dall-Kirkham of the analyzer accomplished an eight to one reduction in size of the wavefront received by the telescope. The two sampling apertures of the interferometer were positioned in the collimated, reduced output of the primary Dall-Kirkham. The secondary Dall-Kirkham converged the illumination

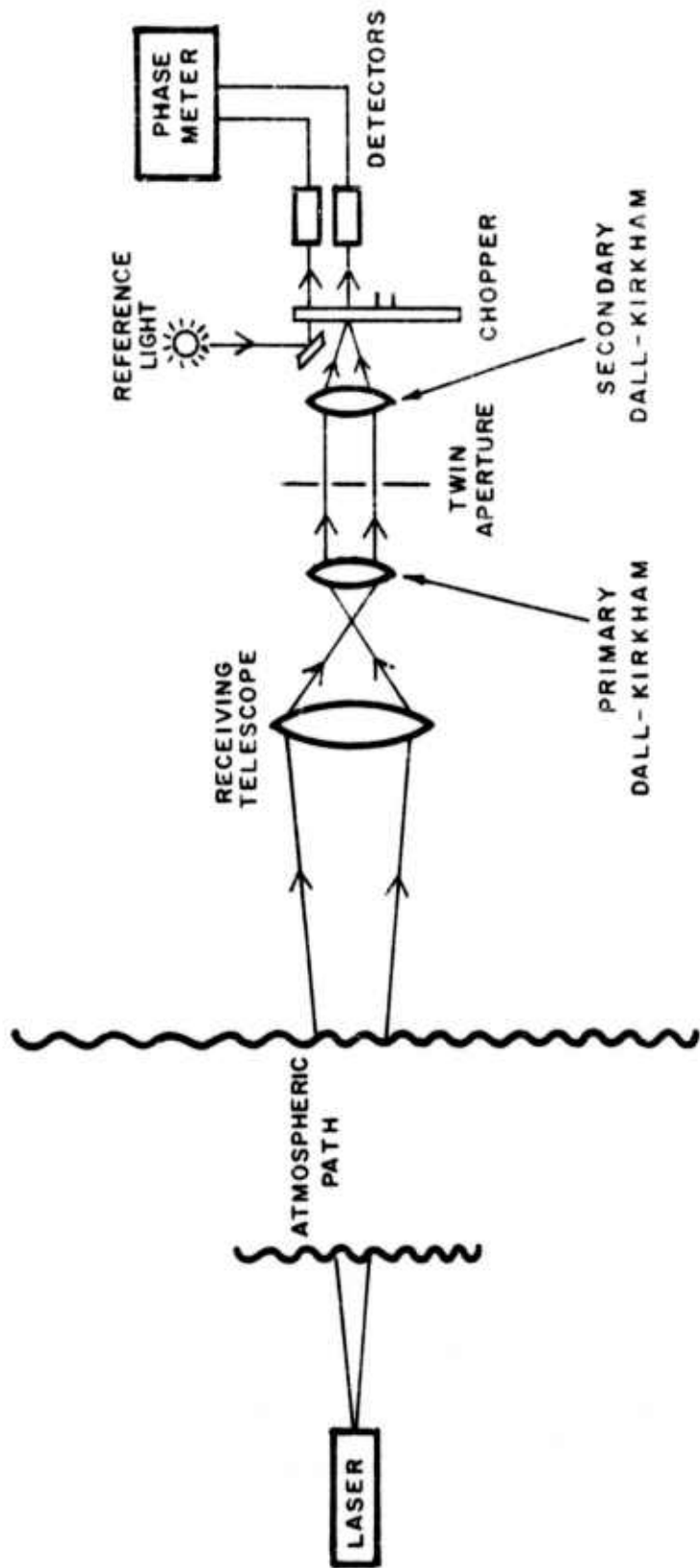


Fig. 3.1. Schematic diagram of the optical analyzer as used to perform the optical phase difference measurements across received laser wavefronts.

of the two apertures and produced an interference pattern at its focal point which was on the surface of a reflective chopping reticle.

### 3.4 Phase Measurement Technique

Appendix A contains an analysis of a typical twin aperture interferometer which shows that the intensity distribution,  $I(x,y,t)$ , of the two-dimensional interference pattern was

$$I(x,y,t) = N \left[ \frac{2J_1[K_1(x^2+y^2)^{1/2}]}{[K_1(x^2+y^2)^{1/2}]} \right]^2 \{1 + \cos[K_2x + \phi(t)]\} \quad (3-1)$$

where  $\phi(t)$  is the time varying optical phase difference between the two apertures

$$N = 4\pi D^2 (d/2)^4$$

$$K_1 = (\pi d / \lambda f)$$

$$K_2 = (2\pi\alpha / \lambda f)$$

$\alpha$  is the aperture separation

$d/2$  is the aperture radius

$D$  is the amplitude of the electric field at each aperture

$f$  is the focal length of the convergent optical system.

The parameters of the interferometer were such that  $K_2 > K_1$ . This resulted in an interference pattern consisting of a large scale circularly symmetrical Airy disc pattern,  $\{[2J_1(K_1(x^2+y^2)^{1/2})]/[K_1(x^2+y^2)^{1/2}]\}$  which was modulated in the x-direction by the higher frequency interference fringes of the term  $[1 + \cos(K_2x + \phi(t))]$ . Equation (3-1) for  $I(x,y,t)$  shows that the position of the fringes in the x-direction was proportional to,  $\phi(t)$ , the optical phase difference of the sampling apertures.

In the optical analyzer, the focal point of the interferometer and hence formation of the interference pattern occurred at the surface of an optical reticle which was rotating at a constant angular velocity of  $w$  radians per second. The reticle, illustrated in Fig. 3.2, was a quartz disc approximately eight inches in diameter. The front surface of the reticle consisted of a periodic pattern of alternately reflecting and absorbing slits of spatial frequency  $K_2$  and of radial length  $L$ . As shown in Fig. 3.2, the interference pattern and reticle were arranged so that the  $x$ -direction of the interference pattern was aligned with the direction tangential to the edge of the reticle.

Rotation of the reticle produced a modulation of the interference pattern intensity which was reflected from the reflective reticle slits to a mercury-cadmium-telluride detector. This modulation was equivalent to multiplication of the interference pattern intensity,  $I(x,y,t)$ , by a reticle function,  $M(x,y,t)$ , to produce the resultant intensity

$$I_1(x,y,t) = I(x,y,t)M(x,y,t). \quad (3-2)$$

The reticle function is approximately an infinite series of square waves in the  $x$ -direction of spatial frequency  $K_2$  which were spatially phase modulated in the  $x$ -direction at a rate corresponding to the tangential velocity of the reticle. Thus, for slits of radial length  $L$  in the  $y$ -direction, the approximate reticle function becomes

$$M(x,y,t) = \left[ \text{SQ}(K_2x + Wt) \left[ U(y+L/2) - U(y-L/2) \right] \right] \quad (3-3)$$

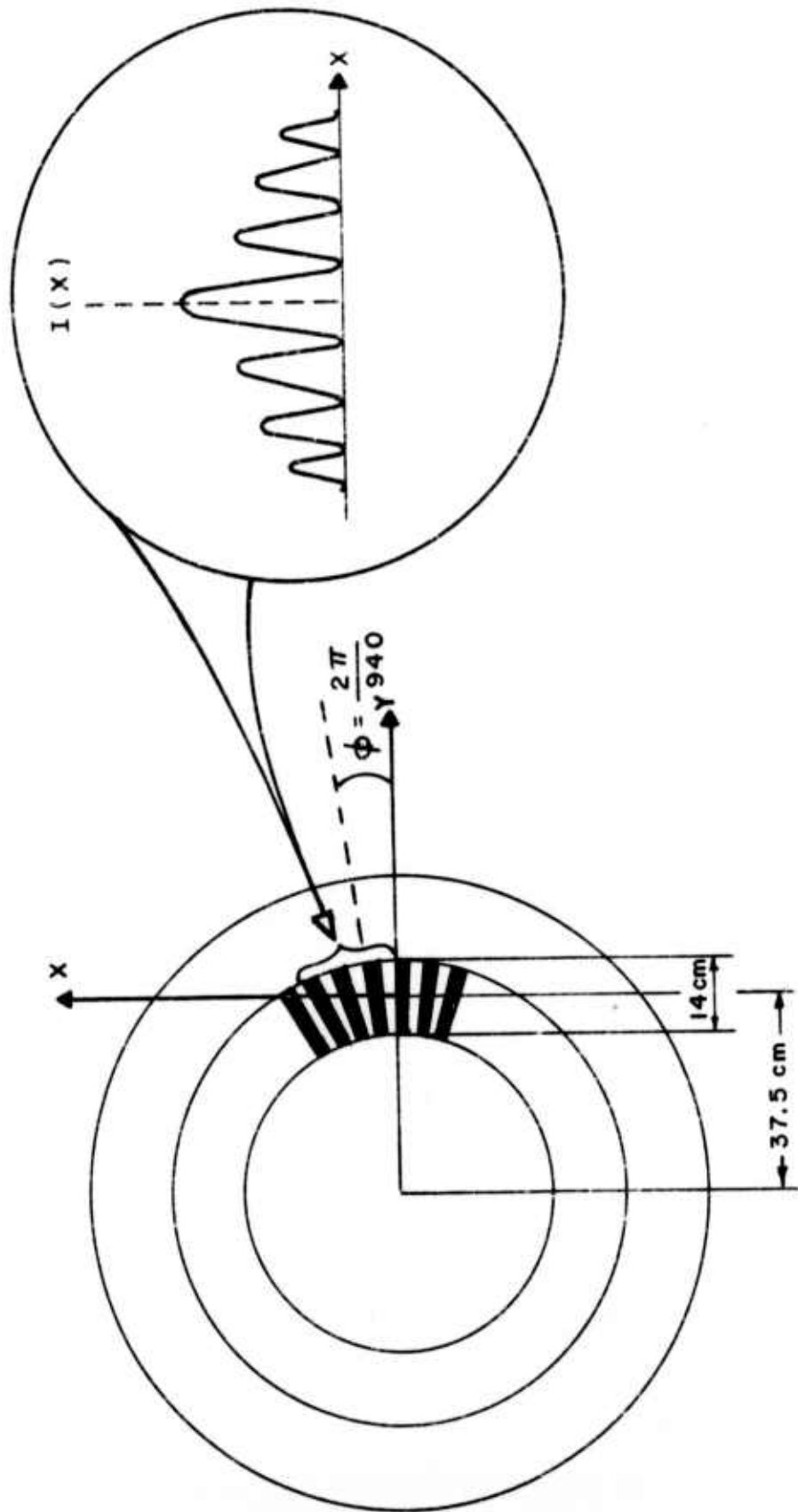


Fig. 3.2. Illustration of the reflective reticle used in the optical analyzer and the spatial intensity distribution of the interference pattern,  $I(x)$ , formed on the reticle surface.

where  $SQ(K_2x)$  is the spatial square wave function of frequency  $K_2$

$R$  = radial distance on reticle surface to the center of the interference pattern

$w$  = constant angular velocity of the reticle in radians per second

$U(y)$  = unit step function in the  $y$ -direction

$W = K_2Rw.$

Appendix B contains an analysis of the error that arises from approximating the reticle function by an infinite series of square waves. There are two errors which occur for each fringe in the interference pattern. The first error is in the location or absolute position of the spatial interval corresponding to that particular  $2\pi$  radian fringe period, and the second error is in the spatial length of each fringe period. For the central fringe in the pattern, the positional and interval length errors are equal and are  $7.44 \times 10^{-4}$  percent of one interval. This is much smaller than the minimum resolution of our phase measurement which was one part in 256. Due to the power of the transmitter, the noise equivalent power level of the infrared detector, and the input noise voltage level of the detector preamplifier; the power level of the seventh fringe was at all times below the minimum detectable signal level. The errors for the seventh fringe therefore will be the largest to effect the resolution of the experiment. The positional error for the seventh fringe is 0.511 percent of one interval and the interval length error is 0.189 percent of one interval. Therefore,

in the worst case the phase resolution is limited to 0.701 percent of one interval or 0.044 radians.

The power received by the infrared detector is the integral over the detector's field of view (FOV) of the product of the modulated intensity  $I_1(x,y,t)$  and one-half the admittance of free space,  $Y_0$ . The instantaneous power received by the detector was therefore

$$P(t) = \frac{1}{2} Y_0 \iint_{\text{FOV}} I_1(x,y,t) dydx.$$

Since the minimum detectable signal level limits the usable field of view of the detector in the interference pattern plane to the range  $-B/2 < x, y < +B/2$ , the expression for the instantaneous power becomes

$$P(t) = \frac{1}{2} Y_0 N \int_{-B/2}^{+B/2} \int_{-B/2}^{+B/2} \left[ \frac{2J_1[K_1(x^2+y^2)^{1/2}]}{[K_1(x^2+y^2)^{1/2}]} \right]^2 [1 + \cos[K_2x + \phi(t)]] [SQ(K_2x + Wt)] [U(y+L/2) - U(y-L/2)] dydx. \quad (3-5)$$

The preceding integral can be simplified by the following assumptions which apply to this particular case. The square wave function can be approximated by its fundamental term  $\cos(K_2x + Wt)$ . The two-dimensional Airy function,  $\{[2J_1(K_1(x^2+y^2)^{1/2})]/K_1(x^2+y^2)^{1/2}\}^2$ , can be approximated by a constant,  $A$ , in both directions since the effective field of view of the detector at the reticle was spatially limited to a small, centrally located, portion of the Airy function, and since absolute intensity was not of importance.

The simplified integral for the instantaneous power received by the detector is

$$P(t) = \frac{1}{2} Y_0 N A \int_{-B/2}^{+B/2} \int_{-B/2}^{+B/2} [1 + \cos(K_2x + \phi(t))] [\cos(K_2x + Wt)] [U(y+L/2) - U(y-L/2)] dydx \quad (3-6)$$

which after the y-integration reduces to

$$P(t) = \frac{1}{2} Y_0 N A B \int_{-B/2}^{+B/2} [1 + \cos(K_2 x + \phi(t))] [\cos(K_2 x + Wt)] dx \quad (3-7)$$

since  $L/2 > B/2$ .

Assuming the field of view in the x-direction encompassed an integer number of cycles, the result of the x-integration is

$$P(t) = \frac{1}{2} Y_0 N A B (2\pi/K_2) \cos[\phi(t) - Wt] \quad (3-8)$$

or

$$P(t) = P \cos[\phi(t) - Wt]. \quad (3-9)$$

The output voltage of the detectors is linearly related to the input power by the detector responsivity, R. The detector output voltage is therefore

$$V(t) = RP(t) \quad (3-10)$$

or

$$V(t) = RP \cos[\phi(t) - Wt]. \quad (3-11)$$

These equations show that the detector input power and output voltage were both temporal sinusoidal functions phase modulated by the optical phase difference at the interferometer aperture.

A phase reference signal was obtained from the analyzer by detecting the output of a fixed visible-wavelength reference light source, the intensity of which was also modulated by the chopping reticle. The resulting reference signal voltage was

$$V_{\text{ref}}(t) = I \cos[\phi_{\text{ref}} - Wt]. \quad (3-12)$$

The two signals from the optical analyzer, the phase measurement signal and the reference signal, were then processed in real time by a hard-wired digital phase difference meter which measured

the phase difference between the reference channel signal and the phase-modulated measurement channel signal. Fig. 3.3 is a simplified block diagram of the digital phase difference meter. The input section of the meter performs dual channel analog signal conditioning by the use of bandpass filters and high gain comparators with hysteresis. The output signals of the bandpass filters were  $V_m = P\cos[\phi(t)-Wt]$  for the measurement channel and  $V_{ref} = I\cos[\phi_{ref}-Wt]$  for the reference channel. The comparators convert these sinusoidal signals into fast rise time square waves suitable for use with digital circuits for the following digital phase difference measurement. The output signals from the comparators are the square waves  $V_m = SQ[\phi(t)-Wt]$  and  $V_{ref} = SQ[\phi_{ref}-Wt]$  for the measurement and reference channels, respectively. These square waves are then processed by two negative-edge-triggered, J-K flip-flops and an Exclusive-OR gate to produce a pulse whose width equals the time interval corresponding to the phase difference between the two channels. This pulse then controls an AND gate, permitting a particular number of clock pulses to propagate through the AND gate to the phase measurement counters. Thus, the number of clock pulses reaching the phase measurement counters corresponds to the Exclusive-OR gate pulse width which is equal to  $[\phi(t)-\phi_{ref}]$ , the difference between the time varying optical phase difference and a constant arbitrary phase reference.

At this point the phase meter performs two different simultaneous phase measurements; one of the intra-cycle, within  $2\pi$  radians,

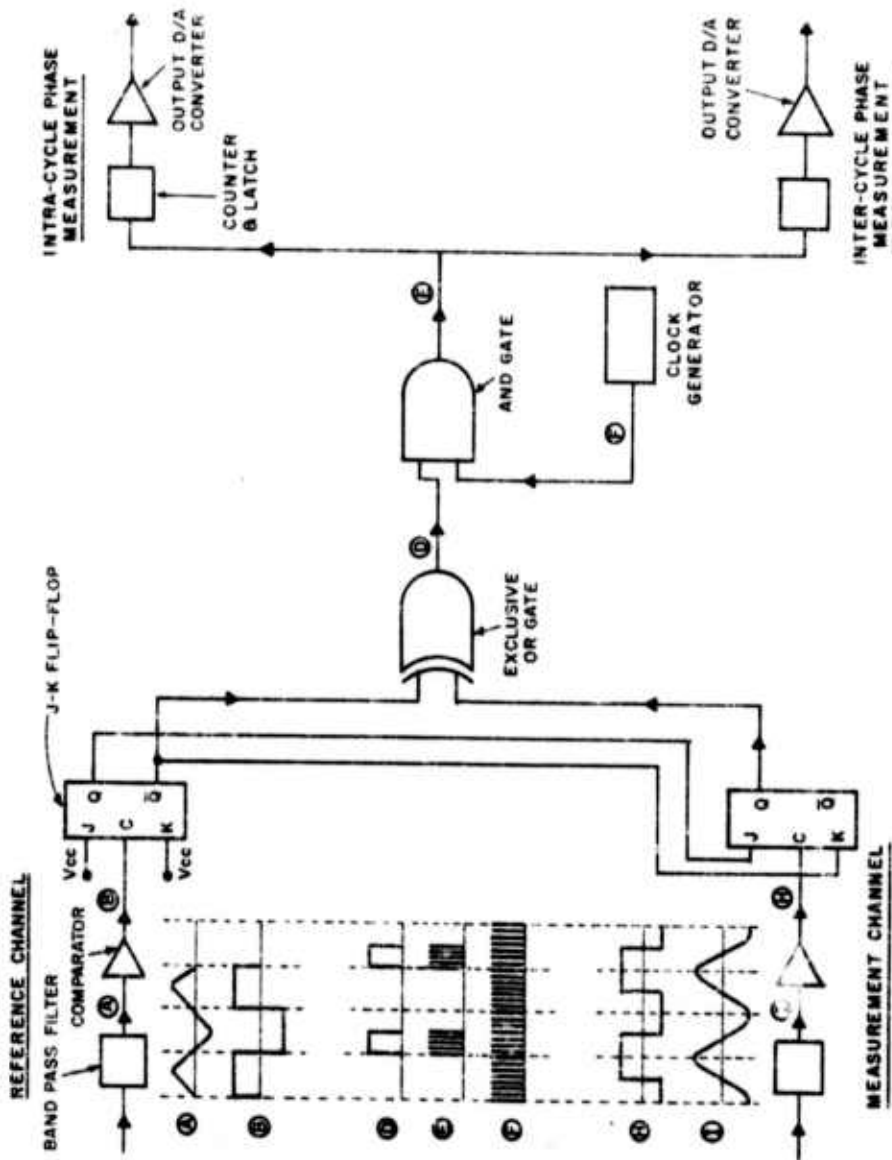


Fig. 3.3. Schematic diagram of the hard-wired digital phase difference instrumentation.

phase difference and one of the inter-cycle, greater than  $2\pi$  radians, phase difference. The intra-cycle phase measurement was performed by a modulo-256 counter and an 8-bit digital to analog converter. The resolution of the intra-cycle phase measurement was eight bits.

The inter-cycle phase measurement was performed by a more complex method shown schematically in Fig. 3.4. The clock pulses representing the phase difference are counted by a modulo-256 counter whose output is converted from digital to analog form by an 8-bit converter. The differential amplifier takes the difference between its two input analog voltages, one representing the current phase difference count and the other representing the previous phase difference count which was stored by the sample-and-hold circuit. The difference between the present and previous phase counts is compared to a threshold level by the analog comparator. When the phase difference exceeds  $2\pi$  radians the input to the modulo-256 counter exceeds 256, the  $2\pi$  level, and the counter continues counting the phase difference starting from zero again. Due to the rapid sample rate at which the measurement is performed, in one cycle for the reference channel the measurement channel phase cannot change more than several degrees. This results in a large difference between the present and previous phase measurements when a slip of one cycle occurs. This difference exceeds the threshold level of the comparator and causes its output to change state. The comparator output is then differentiated by a high pass filter to form a fairly sharp pulse which in turn causes the output up-down

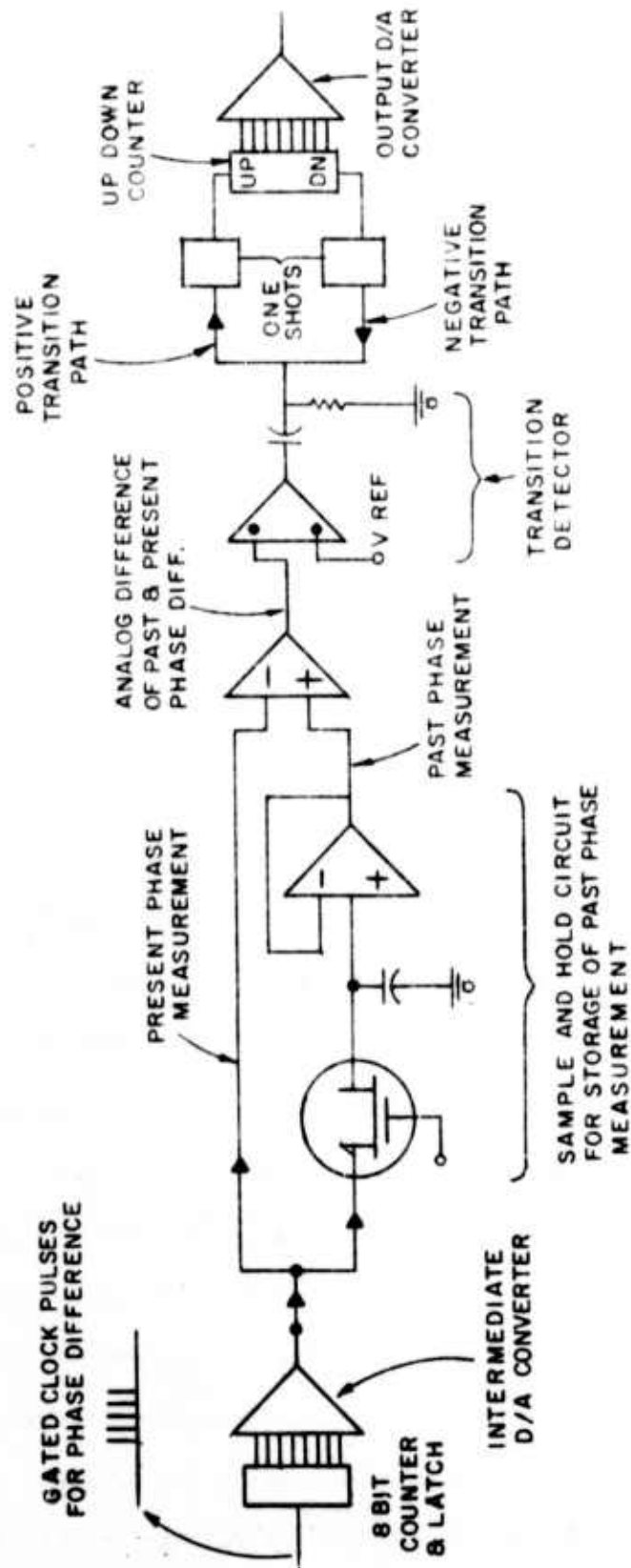


Fig. 3.4. Schematic diagram of the inter-cycle phase measurement circuitry.

counter to count up or down by one, the direction of the count dependent upon the direction of the phase slip. This counter is not reset at each sample and hence represents the long term inter-cycle phase difference. The output counter is also connected to a digital-to-analog converter which has a resolution of six bits. When propagation conditions caused the dynamic range of the phase measurement to increase beyond  $2\pi$  radians, it was then possible to combine these two separate measurements to yield the required dynamic range.

### 3.5 Meteorological Measurements

Simultaneous to the performance of the optical experiments, measurements were made of gross meteorological parameters and of the microstructure of the temperature field.

The wind direction and speed are important in determining scaling parameters for analyzing optical data. Wind direction was measured with a Packard-Bell low-inertia wind vane system which had a -3dB point at 5Hz. Wind direction measurements were made with Packard Bell six-cup anemometers which had a -3dB point also at 5Hz.

Microtemperature was measured on a single probe constructed at RADC according to the design of Ochs<sup>(9)</sup> at NOAA. The RADC sensors are platinum wire 2.5 $\mu$ m in diameter and about 2 mm in length. The 3db point of such a probe is about 500 Hz in 5m/sec winds, and that is certainly adequate for expected fluctuation rates. The sensor is connected as one leg of a Wheatstone Bridge. Temperature changes sensed by the probe cause a proportional imbalance voltage at the bridge. The imbalance voltage is amplified by a gain

of  $1.1 \times 10^4$  and then recorded on analog tape for later processing. As the probe draws only about 450 $\mu$ a current, it operates as a cold-wire sensor for wind speeds exceeding 0.5 m/sec. A much more extensive description of the microthermal system is given in a report by Greenwood and Tarazano.<sup>(10)</sup>

### 3.6 Data Recording and Reproduction

When the experiments were conducted, the two channels of optical phase difference data from the digital phase meter and all the meteorological data were recorded on an Ampex analog instrumentation tape recorder. The frequency-modulation mode of recording was used at tape speeds of either 7.5 or 15 inches per second which yielded recorder bandwidths of 0 Hz to 2500 Hz and 0 Hz to 5000 Hz, respectively.

The data was later replayed on the tape recorder for digitization by a Digital Equipment Corporation PDP-8 computer with a 12-bit analog-to-digital converter. Prior to digitization, the signals were filtered to prevent aliasing with four-pole Butterworth low-pass filters set for the proper antialiasing at the Nyquist frequency.

## Chapter 4

### ANALYSIS OF EXPERIMENTAL DATA

#### 4.1 Introduction

The optical and meteorological data collected during the experiment was initially recorded in analog form. The data recordings were replayed at a later time for statistical and power spectral density analysis.

#### 4.2 Optical Data Analysis

The optical phase difference data was processed to yield estimates of the average temporal power spectral density of the phase difference fluctuations. Most of the optical power spectral density analysis and processing was performed by a fast Fourier transform technique on a digital computer. However, some of the high frequency power spectral density information was obtained by processing the data with a Ubiquitous Spectrum Analyzer and Averager system. This chapter will describe the analysis procedures and the associated confidence limits of the resulting data for both types of power spectral density processing.

For the fast Fourier transform processing, the analog data was converted to 12-bit digital words and then stored on digital magnetic tapes by a Digital Equipment Corporation PDP-8 computer equipped with a 12-bit analog-to-digital converter. These digital data tapes were then processed by a Fortran IV fast Fourier transform

algorithm on a Honeywell-645 computer. The Honeywell computer used a 36-bit floating-point arithmetic format which had 27 binary bit significance in the mantissa of the floating-point words. There are three major factors affecting the accuracy of the processed power spectral density data. These accuracy determining factors are errors that arise from the digitization and computer processing of the original analog data.

The three errors in the fast Fourier transform algorithm processing all arise from computer and analog-to-digital converter rounding of numerical values of infinite precision to values with finite precision. The error due to rounding by the 12-bit analog-to-digital conversion of the initial data,  $x(nT)$ , may be represented by an additive noise,  $e(nT)$ , which has a uniform probability distribution, zero mean, variance of one-twelfth of one bit, and which is uncorrelated between samples. The input to the algorithm is then  $x(nT) = x_0(nT) + e(nT)$  where  $x_0(nT)$  is the noise free input rounded to 12 bits. The evaluation of the propagation of this error through the fast Fourier transform algorithm by analytical means is a difficult task. An experimental test of the effects of this error on the dynamic range of the output power spectra can be conducted using a "white noise" generator and filters of known characteristics. This test was not conducted. However, the experimental data which was random, Gaussian distributed, and not white but smoothly filtered, typically exhibited a linear dynamic range of 63 dB.

The remaining two computer generated errors are due to rounding all multiplication products and multiplication coefficients to produce

27-bit mantissas. For a typical radix-two fast Fourier transform algorithm performed with floating point arithmetic, the variance of the error in the transformed data which arises from the rounding of the multiplication products has been shown (7) to be

$$\sigma_{E,RO}^2 = \frac{2}{3} v N 2^{-2b} \sigma_x^2 \quad (4-1)$$

where  $N = 4096$ , the number of points in the input sequence

$$v = \log_2(N)$$

$b = 27$ , the number of bits in the mantissa of the floating point word

$\sigma_x^2$  = the variance of the input sequence.

Since for the experimental data the maximum input signal variance was  $3.2 \times 10^{+5}$  bits squared, the maximum root-mean-square output error due to rounding of multiplication products was approximately 0.008 bits.

The variance of the error in the transformed data due to rounding of multiplication coefficients has been shown (7) to be

$$\sigma_{E,C}^2 = \frac{1}{6} v N 2^{-2b} \sigma_x^2, \quad (4-2)$$

which for the case of  $N = 4096$  reduces to

$$\sigma_{E,C}^2 = \frac{1}{4} \sigma_{E,RO}^2. \quad (4-3)$$

The root-mean-square error in the transformed sequence due to coefficient rounding is approximately 0.002 bits. Therefore, considering both multiplication product rounding and coefficient rounding, the root-mean-square output error was less than one bit.

In summary, for the fast Fourier transform processing, the analog-to-digital converter round-off error was experimentally

determined to limit the dynamic range of the processed spectra to 60 dB, or approximately ten bits. The error generated by the rounding of both the multiplication products and the multiplication coefficients in the algorithm was shown to introduce a root-mean-square error of less than one bit in the 27-bit mantissas of the transformed data. Therefore, the analyzed spectra have a dynamic range limited to approximately 60 dB or ten bits by propagation of the analog-to-digital converter round-off error through the algorithm.

Some of the experimental power spectral density data showed a large spread between individual spectral curves at low frequencies. As discussed in chapter 5 this spectral spread is due to the large, random wind direction fluctuations. To conclude that the spread of the low frequency spectra was due to the wind direction fluctuations, it was helpful to derive appropriate confidence or expectation intervals for the spectra based on the assumptions of stationarity and a chi-square distribution for averaged spectral values. The confidence limits are due to the fact that the resulting processed power spectral density values,  $P_n^2(f_o)$ , are random variable estimates of the true power spectral density,  $W(f_o)$ , of the initial process. Each power spectral density estimate,  $P_n^2(f_o)$ , is actually a random variable defined as the sample mean of a set of discrete, random power spectral density values by

$$P_n^2(f_o) = \frac{1}{n} \sum_{K=1}^n p_k^2(f_o) \quad (4-4)$$

where  $p_k^2(f_o)$ ;  $K = 1, 2, \dots, n$  is the set of random variables of measured power spectral density values

$P_n^2(f_0)$  is the sample mean power spectral density value estimate.

By making suitable assumptions it is possible to develop an approximate, general criterion for the confidence limits of the estimate which does not require knowledge of the statistics of the original process. The original process is assumed to be stationary, Gaussian distributed, and to possess a relatively smooth power spectrum. Hence, the sample mean power spectral density estimates will be chi-square distributed random variables.

The probability statement that defines the interval about  $P_n^2(f_0) = Y$ , the sample mean estimate, in which we will find the true or theoretical power spectral density value,  $W(f_0)$ , with a probability of 0.8 is

$$\text{Prob} [(Y/c_{10}) < (W(f_0)) < (Y/c_{90})] = 0.8 \quad (4-5)$$

Fig. 5.2 illustrates the use of this probability statement by showing one experimental power spectral density curve and its associated 80 percent confidence intervals. The size of the confidence interval decreases for higher frequencies because a larger number of individual power spectral values were used to form the sample mean estimate.

The probability statement defining the interval about  $W(f_0)$ , the true power spectral density value, in which we expect to find 80 percent of the power spectral density estimates,  $P_n^2(f_0)$ , is

$$\text{Prob} [(C_{90}W(f_0)) < Y < (C_{10}W(f_0))] = 0.8. \quad (4-6)$$

The use of this probability statement is illustrated in Figures 5.3 and 5.6 where the 80 percent expectation intervals about the theoretical power spectral curve are shown.

For the 10 percent and 90 percent confidence limits with which we are concerned, the quantity  $C_p$  is tabulated<sup>(8)</sup> for  $n < 30$ . The equations given in this reference show that suitable approximations for  $C_p$  when  $n \geq 30$  are

$$C_{10} \approx 1.0 + (1.81/\sqrt{n}) \quad (4-7)$$

$$C_{90} \approx 1.0 - (1.81/\sqrt{n}) \quad (4-8)$$

It should be noted that the preceding assumptions of stationarity and a chi-square distribution of power spectral density estimates cause these general case confidence limits to be approximations whose applicability depends upon the degree of adherence to the above restrictions. Hence, for some of the data which is widely distributed without a chi-square distribution of power spectral values, the confidence limits indicated are not representative of the true sample mean and variance.

The fast Fourier transform and power spectral density computer program calculates 2,048 discrete power spectral values. The discrete spectral values occur at intervals of  $1/4,096$  of the sample rate over the range of zero hertz to one-half of the sample rate. The computer program then condenses these 2,048 spectral values into a set of 32 new values which are equally spaced along a logarithmic abscissa or frequency axis. These new values are formed by averaging an appropriate number of the initial 2,048 values in the regions centered at each of the 32 values. Table 4.1 lists the center frequencies corresponding to each of the 32 discrete intervals for the sample frequency of ten hertz which was used for the low frequency data.

Table 4.1

Data Pertaining to the Low-frequency Power  
Spectral Density Curves

Center Frequency	Number of Points Averaged	80% Confidence Limit Factors	
		C <sub>90</sub>	C <sub>10</sub>
0.0024	1	0.0158	2.706
0.0049	1	0.0158	2.706
0.0073	1	0.0158	2.706
0.0098	1	0.0158	2.706
0.0122	1	0.0158	2.706
0.0146	1	0.0158	2.706
0.0171	1	0.0158	2.706
0.0220	3	0.1967	2.084
0.0293	3	0.1967	2.084
0.0366	3	0.1967	2.084
0.0464	5	0.322	1.847
0.0586	5	0.322	1.847
0.0732	7	0.405	1.717
0.0903	7	0.405	1.717
0.1123	11	0.507	1.57
0.1416	13	0.542	1.52
0.1782	17	0.593	1.46
0.2222	19	0.613	1.43
0.2783	27	0.671	1.36
0.3491	31	0.675	1.33
0.4370	41	0.717	1.28
0.5469	49	0.741	1.26
0.6812	61	0.768	1.23
0.8521	79	0.796	1.20
1.0596	91	0.810	1.19
1.3159	119	0.834	1.17
1.6455	151	0.853	1.15
2.0605	189	0.868	1.13
2.5732	231	0.881	1.19
3.2202	399	0.909	1.09
4.0259	361	0.905	1.10
4.7339	218	0.877	1.12

The table also lists the number of points averaged over the 32 intervals and the resulting 10 percent and 90 percent confidence limits for the resulting 32 mean spectral values. The tabulated confidence limit values are the factors by which the experimental, mean spectral values would be divided to yield the range in which we have 80 percent confidence of finding the true or theoretical power spectral density values.

To reduce the large confidence limits which exist at the lowest frequencies, individual power spectral curves were averaged together. These final mean power spectral curves for each day of experimental data are presented in chapter 5 and error bars for the 80 percent confidence limits are also shown.

The optical high frequency data was analyzed with a Federal Scientific Corp. Ubiquitous Spectrum Analyzer (Model UA-10A) and Averager (Model 1010). The Ubiquitous Analyzer performs a direct power spectral measurement by means of a narrow bandpass filter and power detector technique. However, the Ubiquitous Analyzer had a linear dynamic range of only 40 dB. Therefore, the data had to be divided into segments whose spectrum did not exceed this 40 dB range. For this reason only the 40 dB high-frequency portion of the spectrum was processed with the Ubiquitous Analyzer. It was then possible to process the entire lower portion of the data's spectrum with the computer fast Fourier transform techniques which had a 60 dB dynamic range. The high-frequency spectral measurements were performed by averaging 512 individual spectra to produce the final mean spectrum.

The resulting mean spectra had, therefore, 512 degrees of freedom and the corresponding upper and lower confidence limits are 1.08 and 0.92 times the spectral values. The corresponding error bars are relatively small and have not been shown on the spectral curves.

#### 4.3 Meteorological Data Analysis

The meteorological data processing consisted of computing the sample mean and sample variance of the recorded wind speed and wind direction data, and computing the power spectra of the microtemperature fluctuations.

The processing of the wind speed data was straight forward. The data was replayed from the analog tape recordings and digitized by the PDP-8 computer at a sample rate of approximately ten hertz. The wind speed systems have a frequency response of approximately 5.0 Hz which was used as the anti-aliasing filter. Real time calculation of the sample mean,  $\eta$ , and sample variance,  $\sigma^2$ , was performed with the computer according to the formulas

$$\eta = \frac{1}{N} \sum_{i=1}^N X_i \quad (4-9)$$

$$\mu^2 = \frac{1}{N} \sum_{i=1}^N (X_i^2) \quad (4-10)$$

$$\sigma^2 = \mu^2 - \eta^2 \quad (4-11)$$

where  $\mu$  is the second moment of the sampled data.

The wind direction data processing was performed in the same manner as was the wind speed processing except that a different computer program was required to perform the calculations. The wind direction transducer represented wind directions of 0° to 360° by an

analog output voltage of zero to five volts. Therefore, when the wind direction fluctuated about the  $0^{\circ}$ ,  $360^{\circ}$  crossover point, the output voltage fluctuated from zero to five volts. If the previous formulas for sample mean and variance were used for this type of data, incorrect values for  $\bar{\eta}$  and  $\sigma^2$  would result. Due to this anomaly, a special program was required to calculate the mean wind direction.

The mean wind direction program sectioned the digitized wind direction data into the four quadrants of the compass circle, counted the number of samples per quadrant and calculated the mean wind direction per quadrant. To better characterize the magnitude of wind direction fluctuation, values for the mean angle per quadrant and the number of samples per quadrant were calculated and displayed nine times per data record. At the end of the data record the mean angle for the entire record was computed by transforming the mean angles for each quadrant to their rectangular components along the quadrant axis, weighting these components by the number of samples per quadrant, and computing the mean angle from their sum. This also permitted characterization of the frequency of the wind direction fluctuations in a crude fashion. A typical computer printout for a day which had large wind direction fluctuations is shown in Table 5.2.

The power spectral analysis of the microthermal signals utilized the fast Fourier transform approach described in Section 4.2. The major difference is that the Ubiquitous Spectrum Analyzer was used in the high frequencies there, but the digital computer is used for the high frequency

results in the microthermal analysis. The number of points averaged together for the high frequencies is 64 times the tabulated values in Table 4.1. The center frequencies are also shifted by a factor of 40. The resultant confidence limits may be easily calculated via equations (4-7) and (4-8).

## EXPERIMENTAL DATA

5.1 Introduction

Experimental measurements of the optical phase difference for 10.6-micron wavelength laser beams and the corresponding meteorological measurements were performed on fifteen days during the months of March, April and May of 1972. Due to a combination of experimental problems and unfavorable weather conditions there remained only five days of acceptable data. The experimental data of two typical days was completely analyzed and will be presented.

The initial analysis of the optical data showed that the low-frequency region of the phase difference power spectrum behaved differently on days of erratic wind direction conditions than on days of steady wind direction. Therefore, data from days of both conditions is included.

5.2 Experimental Data

Optical and meteorological measurements were performed on the 18th of May, 1972 between eleven o'clock in the morning and two o'clock in the afternoon. This was a clear day with a mean temperature of 76°F.

Table 5.1 lists the means and variances of the horizontal wind speed for the four fourteen-minute intervals over which data was recorded. The mean wind speed fluctuated from 1.12 meters per second to 2.5 meters per second with an overall average of 1.6 meters per

Table 5.1

Wind Speed Data for May 18, 1972

Data Record Number	Mean Wind Speed (Meters/Second)	Wind Speed Variance (Meters/Second) <sup>2</sup>
1	1.38	0.276
2	1.14	0.224
3	1.12	0.224
4	1.98	0.397
5	2.53	0.607

second. Thus on this day the wind speed was very low and had significant amount of variance. Table 5.2 of wind direction data for a typical measurement interval shows that the wind direction on this day had large low frequency fluctuations greater than  $270^\circ$  in magnitude. As shown, at times the wind direction varied slowly back and forth across the laser beam propagation path.

Fig. 5.1 shows the complete set of phase difference power spectra measured on this day. There are eight low-frequency spectra each measured over a seven minute time period and four corresponding high-frequency spectra each measured over two of the seven minute periods. At the lower frequencies these experimental spectra exhibit a rising trend and are spread over four decades vertically. This four decade vertical spread is much greater than the spread permitted by the 80 percent confidence limits of these spectra. Fig. 5.2 illustrates this by showing one spectrum from Fig. 5.1 and its 80 percent confidence limits.

Fig. 5.3 contains a graph of the mean experimental spectrum averaged over all the individual spectra of Fig. 5.1. Fig. 5.3 also contains a graph of Greenwood's theoretical spectrum plotted for an outer scale size of two meters, a second moment of the orientation angle of  $0.12$  radians squared, and a mean wind speed perpendicular to the beam of  $0.6$  meters per second. A mean wind speed of  $0.6$  meters per second was used because it gave the best fit between the theoretical and experimental curves. It was necessary to use this method because the large variations in wind direction prohibited

Table 5.2

Mean Wind Direction Data for May 18, 1972;  
Data Record Number 4

	0° to 90°	90° to 180°	180° to 270°	270° to 360°
Degrees =	40.6	163.9	264.0	286.0
# Samples =	1.0	1.0	143.0	855.0
Degrees =	9.9	0.0	268.4	305.9
# Samples =	105	0.0	15.0	88.0
Degrees =	3.8	0.0	0.0	333.7
# Samples =	282	0.0	0.0	718.0
Degrees =	72.6	114.1	264.0	289.4
# Samples =	1.0	2.0	206.0	791.0
Degrees =	58.3	133.1	262.1	274.6
# Samples =	3.0	4.0	451.0	542.0
Degrees =	35.5	119.4	261.5	273.8
# Samples =	3.0	7.0	266.0	724.0
Degrees =	0.0	0.0	250.9	275.3
# Samples =	0.0	0.0	892.0	108.0
Degrees =	158.2	116.4	244.4	276.4
# Samples =	3.0	2.0	850.0	145.0
Degrees =	0.0	0.0	260.5	292.1
# Samples =	0.0	0.0	43.0	957.0

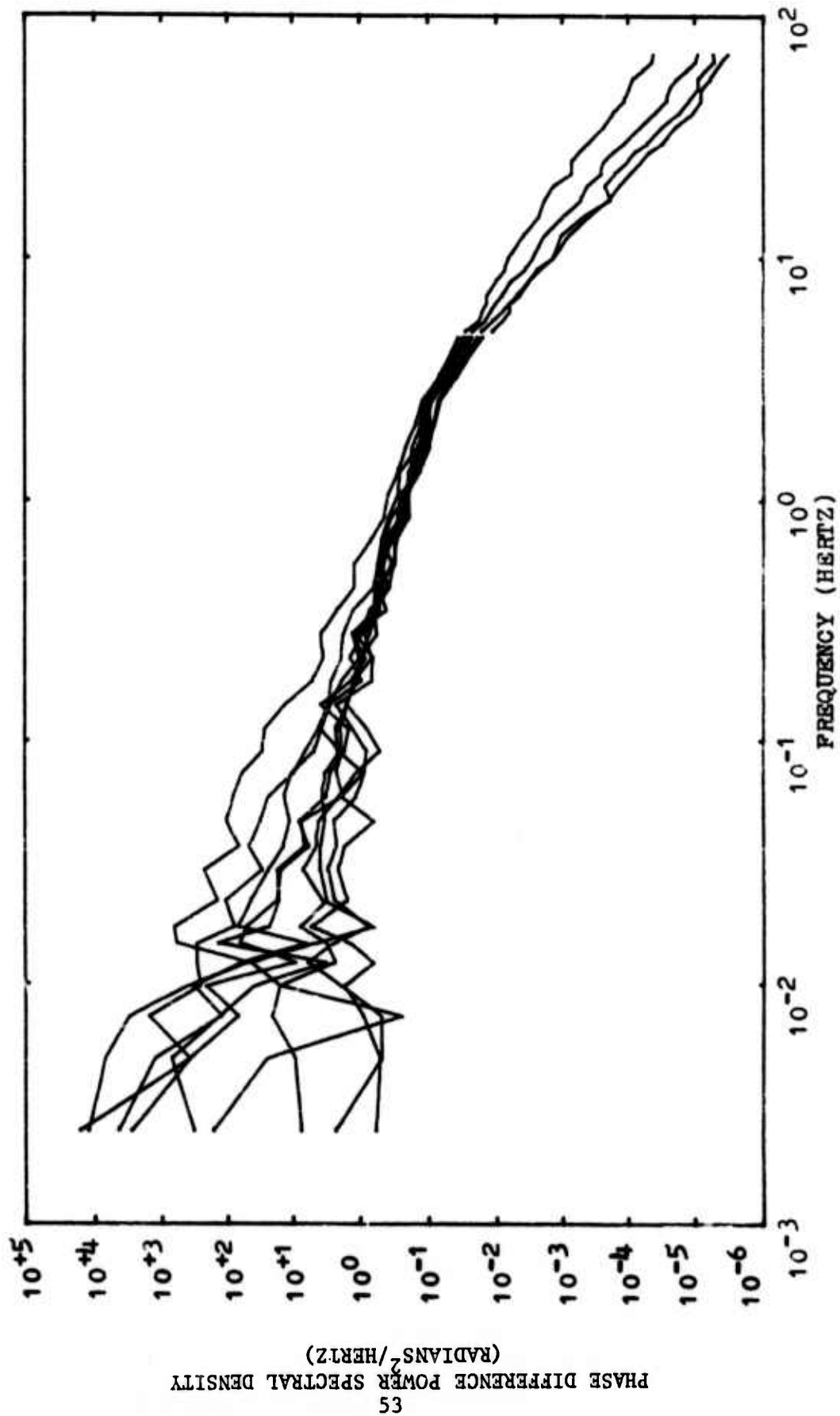


Fig. 5.1. The combined set of high and low frequency experimental phase difference spectra measured on May 18, 1972.

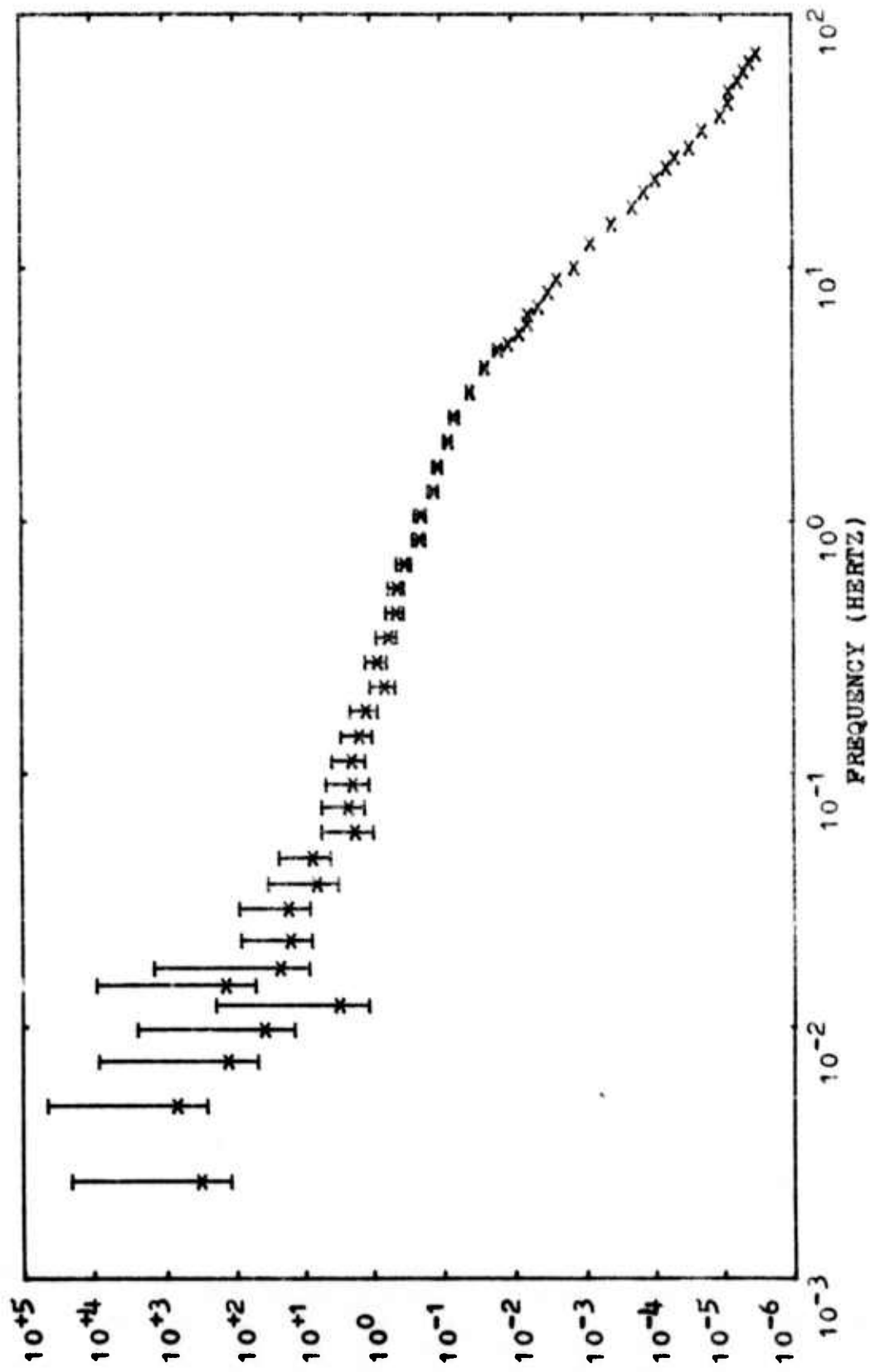


Fig. 5.2. An individual phase difference power spectrum measured on May 18, 1972. The vertical bars indicate the 80 percent confidence intervals about each power spectral value (x x x).

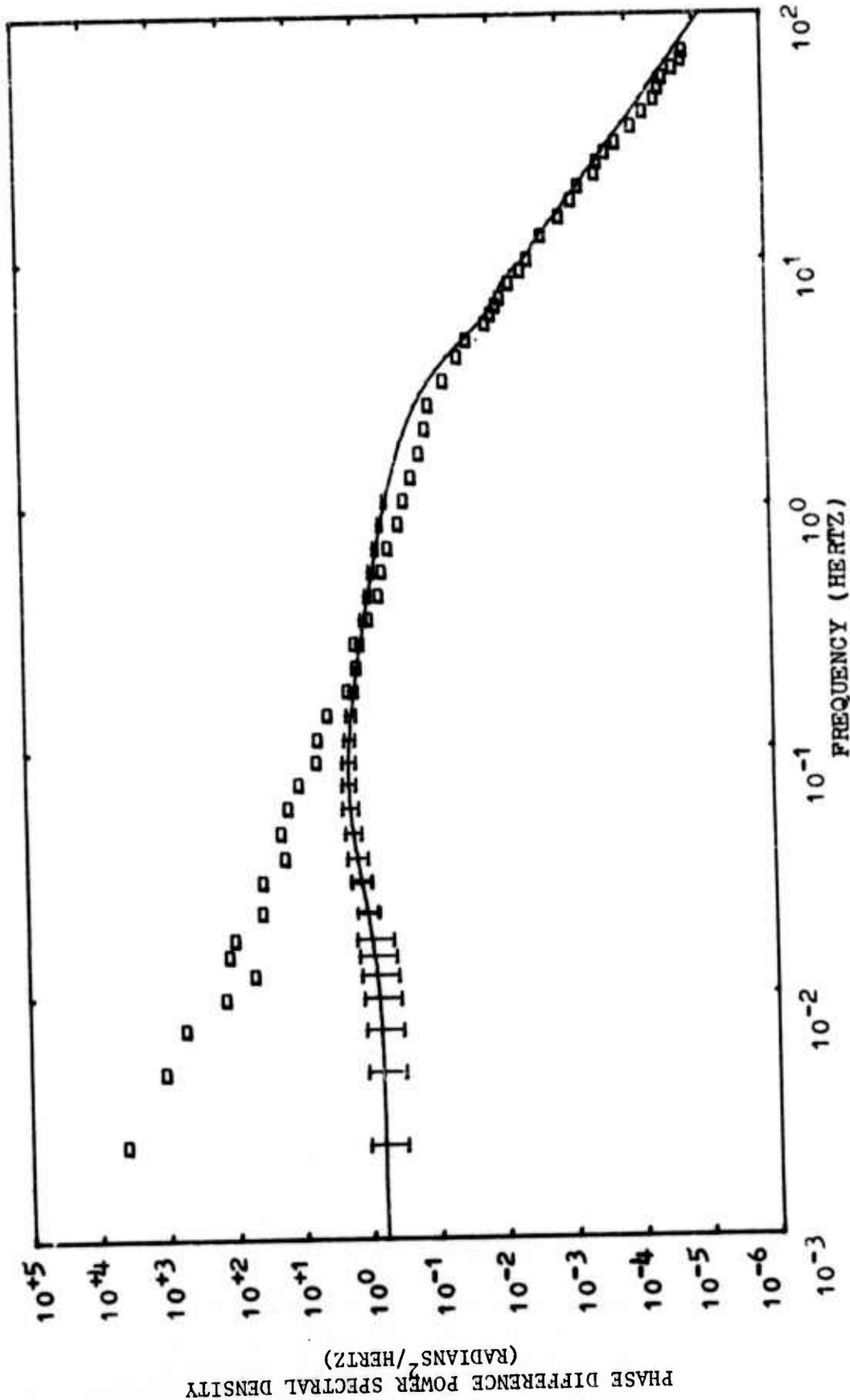


Fig. 5.3. The mean experimental phase difference spectrum ( $\square \square \square$ ) averaged over all the individual spectra of Fig. 5.1. Greenwood's theoretical spectrum for  $v_1 = 0.6$  m/s (solid line) and the appropriate 80 percent confidence limits.

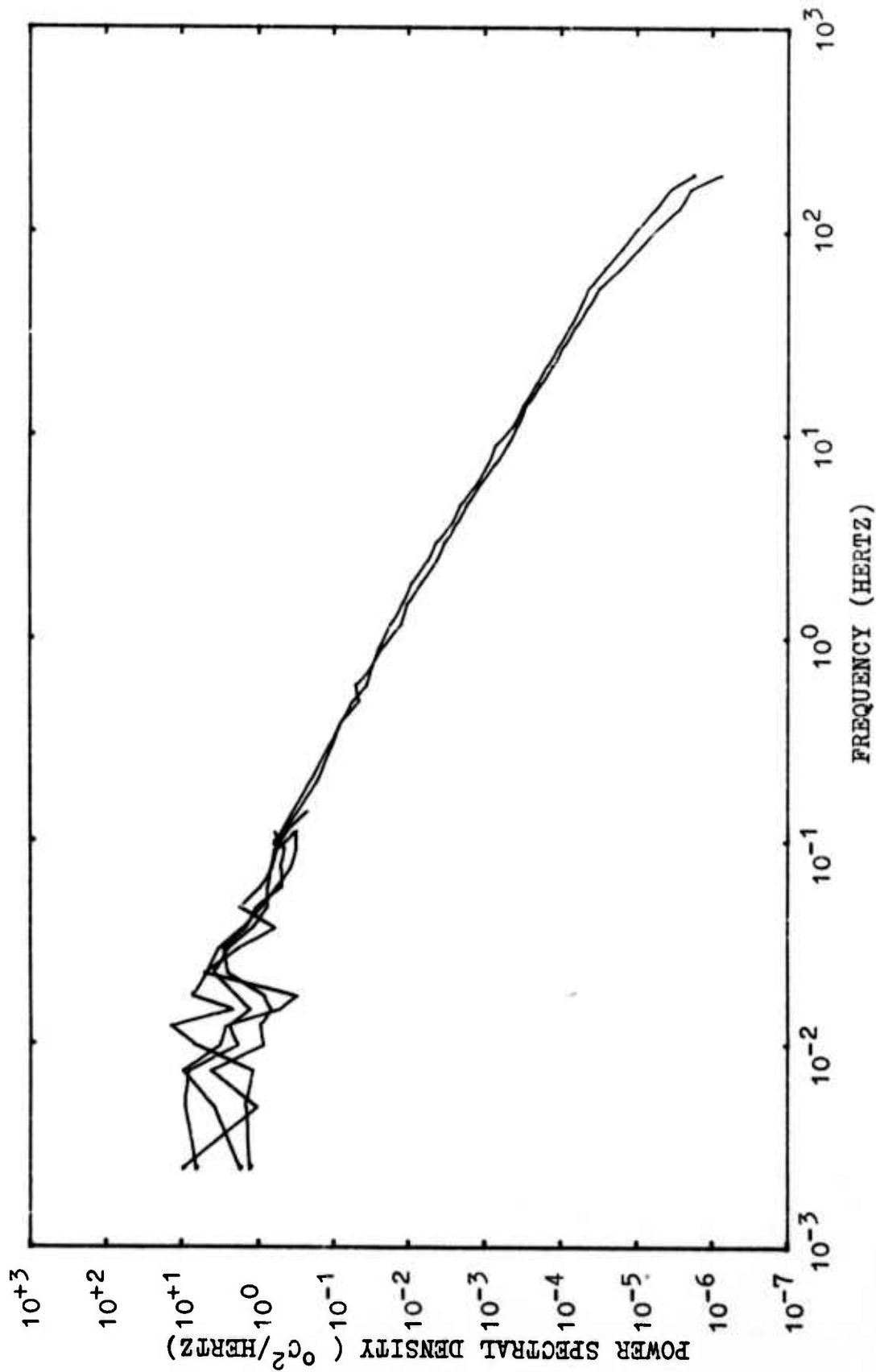


Fig. 5.3a. The combined set of high and low frequency experimental microtemperature spectra measured on May 18, 1972.

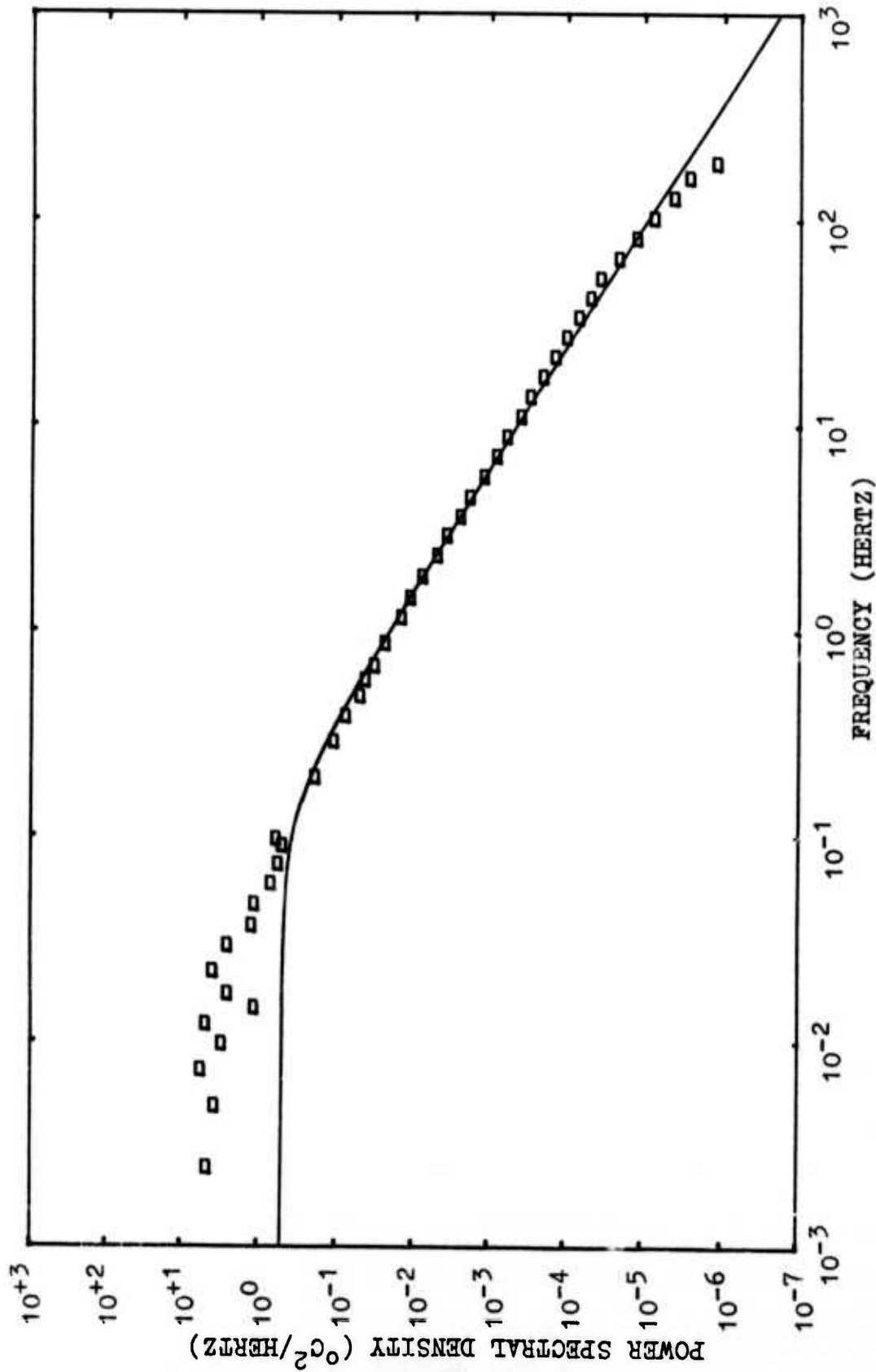


Fig. 5.3b. The mean experimental microtemperature spectrum (O) averaged over all the individual spectra of Fig. 5.3a. Theoretical curve based on von Karman's spectrum, using  $v=2$  m/s and  $L_0=2$  m.

a meaningful determination of the effective perpendicular wind velocity along the entire beam from a single point wind speed and wind direction measurement.

The theoretical and mean experimental curves fit closely together in the high-frequency region where  $f > \sqrt{6}v_{\perp}/2\pi\rho$  or  $f > 3.2v_{\perp}$ . In the medium-frequency region, defined as  $Av_{\perp}/2\pi L_0 < f < \sqrt{6}v_{\perp}/2\pi\rho$  or  $.08v_{\perp} < f < 3.2v_{\perp}$ , the two curves begin to separate vertically by less than a decade. This separation of the two curves at medium frequencies is due to both poorer confidence limits and the same conditions which caused even larger separations in the low frequency region. In the low-frequency region  $f < Av_{\perp}/2\pi L_0$ , the mean experimental curve rises four decades above the flattening level of the theoretical spectrum.

The microtemperature power spectra for May 18, 1973, Figures 5.3a and 5.3b, demonstrate a behavior in the low-frequencies similar to the phase-difference spectrum. The data in Figure 5.3b, indicated by 0's are the averages of the individual curves in Figure 5.3a. The theoretical curve in Figure 5.3b is based on von Karman's spatial spectrum.<sup>(10)</sup> The excess power in the low-frequencies of the microtemperature spectrum insures us that there was no basic error in the measurement of phase-difference.

The separation of the theoretical and experimental spectra at low frequencies is too great to be entirely accounted for by the existing confidence limits. Instead, this separation must be attributed to the large fluctuations in wind direction and to the low and intermittent wind



speed conditions which existed during the measurement of these spectra. For these conditions of wind speed and wind direction, the large-scale spatial anisotropy and non-homogeneity of the turbulence and refractive index fields contribute a significant amount of variance to the level of the spectra at low frequencies.

Consideration of the local terrain as sketched in Figure 5.4 shows the existence of large wooded areas along the north side of the propagation path and immediately behind the transmitter. The development of the aforementioned anisotropic and non-homogeneous turbulence is easily accounted for since at times the wind was from the wooded areas and at other times from the clear fields south of the path. The major difference in turbulence generated in wooded areas as opposed to turbulence from unobstructed level terrain is at low spatial frequencies or large scale sizes. Therefore, during this experiment the fluctuating wind direction and low wind speed conditions produced fluctuations in the spatial distribution of the larger scales of turbulence which were optically measured as low temporal frequency fluctuations of the optical phase difference.

The second set of experimental measurements were performed on the 25th of May, 1972 between eleven o'clock in the morning and one o'clock in the afternoon. This was another clear day for which the mean temperature was 69°F.

The horizontal wind speed for this day was moderate and fairly steady. Over the entire data recording period, the mean wind speed was 5.5 meters per second. Table 5.3 lists the mean values of the wind speed

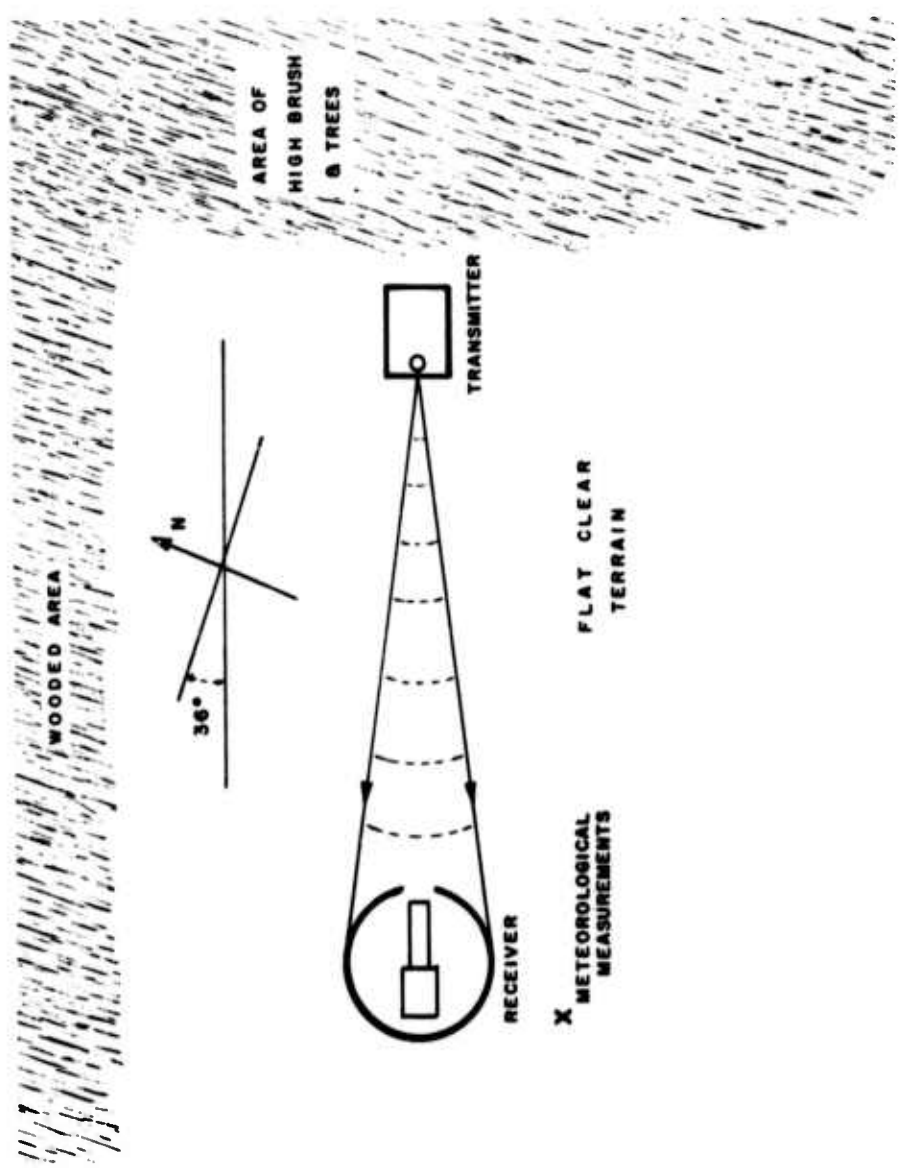


Fig. 5.4. An overhead sketch showing the local terrain surrounding the propagation path.

Table 5.3

Wind Speed and Direction Data for May 25, 1972

Data Record Number	Mean Wind Speed (Meters/Second)	Mean Wind Direction Angle (Degrees from North)	Mean Horizontal Wind Speed Component Perpendicular to Laser Beam (Meters/Second)
1	6.14	82.7	2.96
2	5.93	71.0	1.65
3	5.20	70.8	1.41
4	5.22	71.8	1.73
5	5.32	77.5	2.10

Table 5.4

Mean Wind Direction Data for May 25, 1972;  
Data Record Number 4

	0° to 90°	90° to 180°	180° to 270°	270° to 360°
Degrees =	70.5	90.3	0.0	0.0
# Samples =	849.0	151.0	0.0	0.0
Degrees =	75.98	0.0	0.0	0.0
# Samples =	1000.0	0.0	0.0	0.0
Degrees =	67.14	0.0	0.0	0.0
# Samples =	1000.0	0.0	0.0	0.0
Degrees =	79.63	0.0	0.0	0.0
# Samples =	1000.0	0.0	0.0	0.0
Degrees =	78.43	0.0	0.0	0.0
# Samples =	1000.0	0.0	0.0	0.0
Degrees =	140.0	0.0	0.0	0.0
# Samples =	1000.0	0.0	0.0	0.0
Degrees =	62.96	0.0	0.0	0.0
# Samples =	1000.0	0.0	0.0	0.0
Degrees =	69.2	90.1	0.0	0.0
# Samples =	937.0	63.0	0.0	0.0
Degrees =	64.94	0.0	0.0	0.0
# Samples =	1000.0	0.0	0.0	0.0

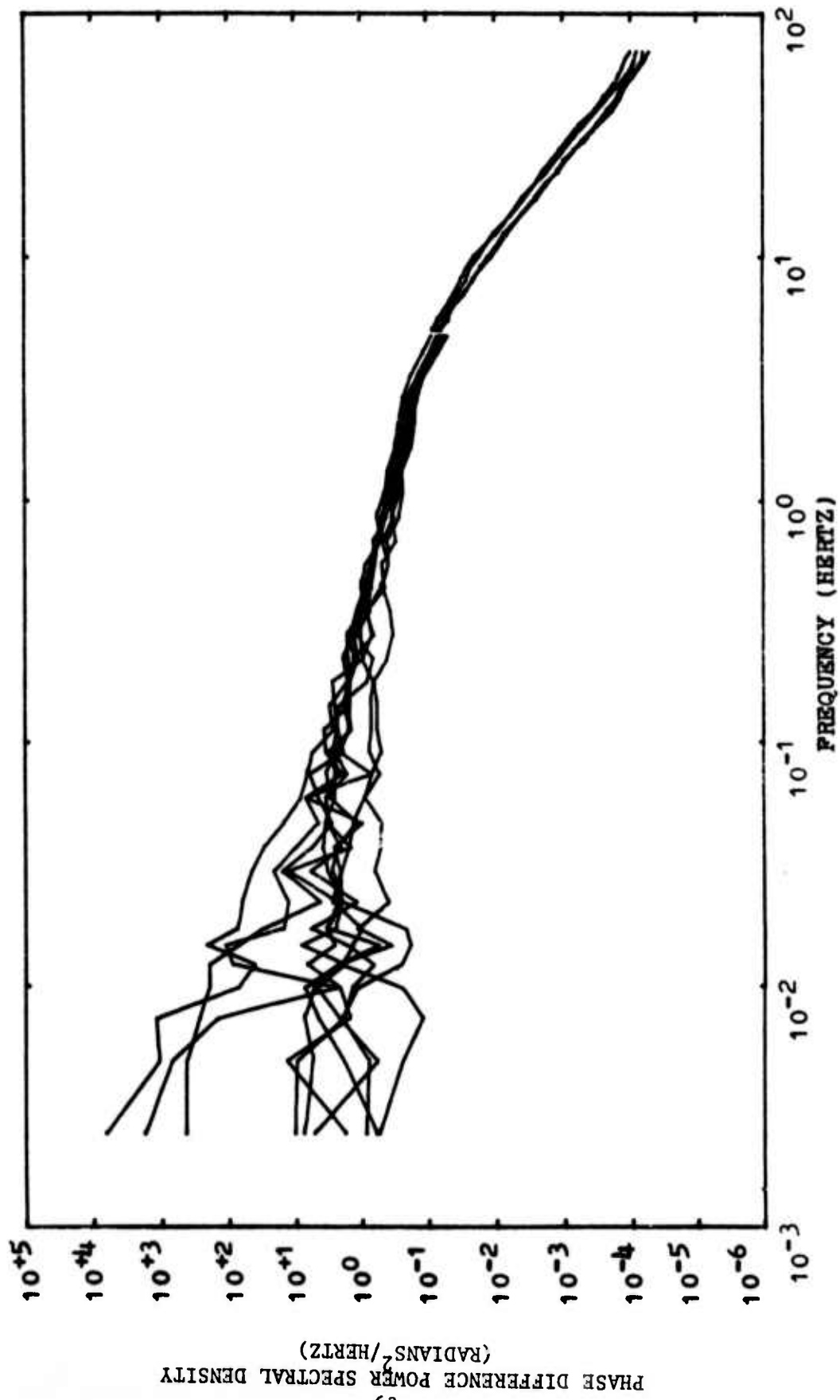


Fig. 5.5. The combined set of high and low frequency experimental phase difference spectra measured on May 25, 1972.

for the five fourteen-minute individual data records. The mean wind direction over the entire data recording period was  $74.76^{\circ}$  from the north or  $112.5^{\circ}$  from perpendicular to the path. Table 5.4 which contains the wind direction data for a typical individual data record shows that the wind direction variance was much less than for the previous data of March 18th.

Figure 5.5 shows the set of experimental spectra measured on May 25, 1972. The ten low-frequency spectra were measured over a seven-minute time period and the five corresponding high-frequency spectra were each measured over two of the seven-minute periods. As clearly illustrated by the graph, seven out of ten of the spectra exhibited the theoretically predicted flattening tendency at low frequencies.

Figure 5.6 shows a mean experimental spectrum averaged over the seven curves which had a flattening trend at low frequencies. This figure also contains a graph of Greenwood's theoretical spectrum with the appropriate 80 percent confidence limits. This theoretical spectrum is for an outer scale of two meters, an orientation angle variance of  $.12$  radians squared, and for a mean wind speed perpendicular to the beam of 1.0 meters per second. This value of mean perpendicular wind speed is one-half the measured value of 1.97 meters per second, but it is the perpendicular wind speed which resulted in the best fit of the curves at high and medium frequencies. The mean wind speed and wind direction measurements were performed about fifty feet from the receiver building, hence the wake effects of the building could be a contributor to the factor of two discrepancy in the

wind speed producing the best fit to the experimental spectrum.

The two spectra fit closely in the high and medium frequency regions. At the low-frequency outer-scale breakpoint, defined as  $f = Av_1/2\pi L_0$ , the two curves begin to separate. In the low-frequency region, both curves show a flattening trend, however, the experimental spectrum settles to a lower value than the theoretical spectrum. In general, however, for this day of moderate wind speed and small wind direction variance the experimental and theoretical spectra showed good agreement.

Figures 5.6a and 5.6b are the microtemperature spectra for the May 25, 1972 mission. Figures 5.6a and b correspond to 5.3a and b in that we have the individual and averaged spectra as well as the theory. Again, excess low frequency power is also present in the microtemperature fluctuations and this supports the phase-difference results.

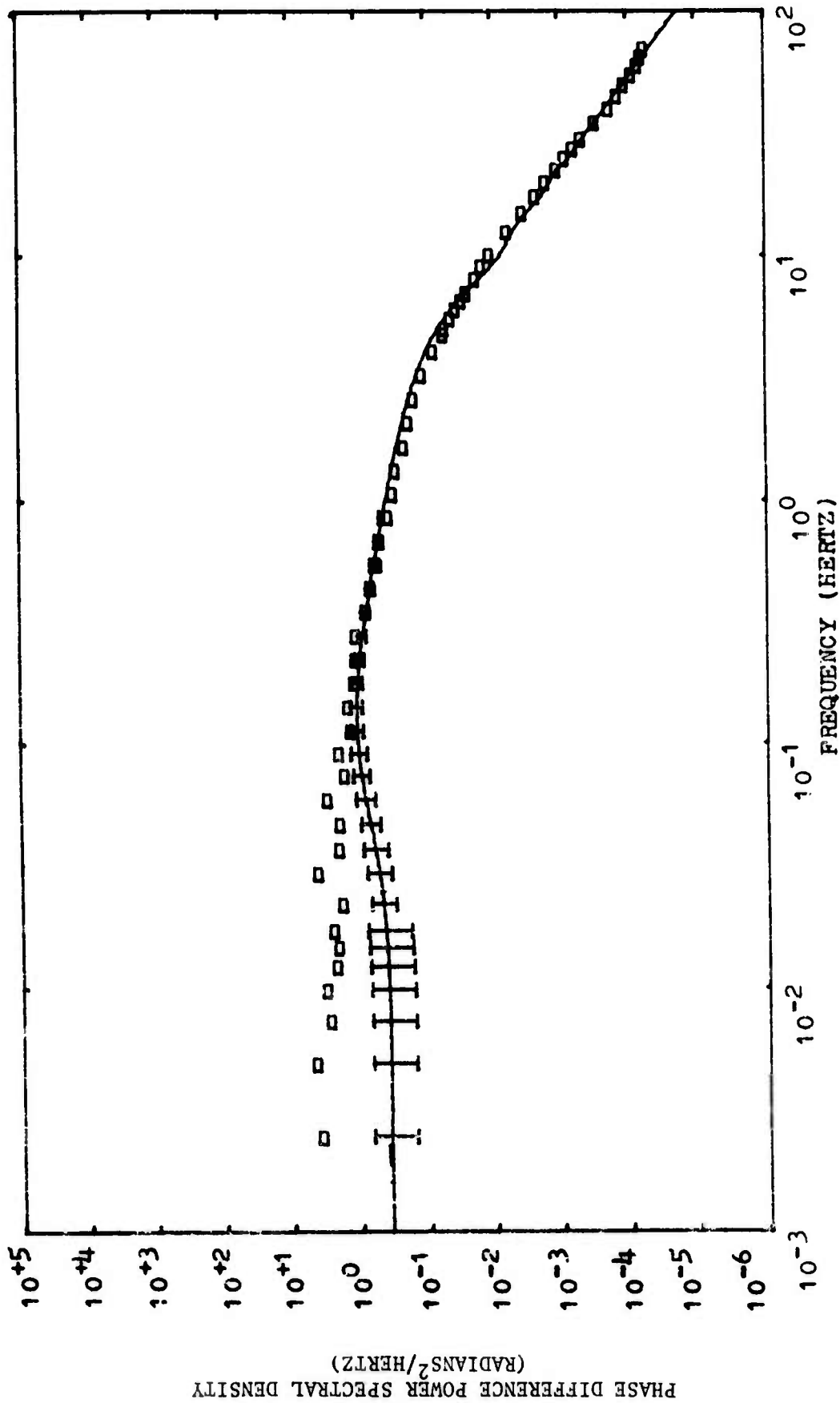


Fig. 5.6. The mean experimental phase difference spectrum ( $\square$ ) averaged over seven out of ten of the individual spectra of Fig. 5.5. Greenwood's theoretical spectrum for  $v_1 = 1.0$  m/s (solid line) and the appropriate 80 percent confidence limits.

Reproduced from  
best available copy.

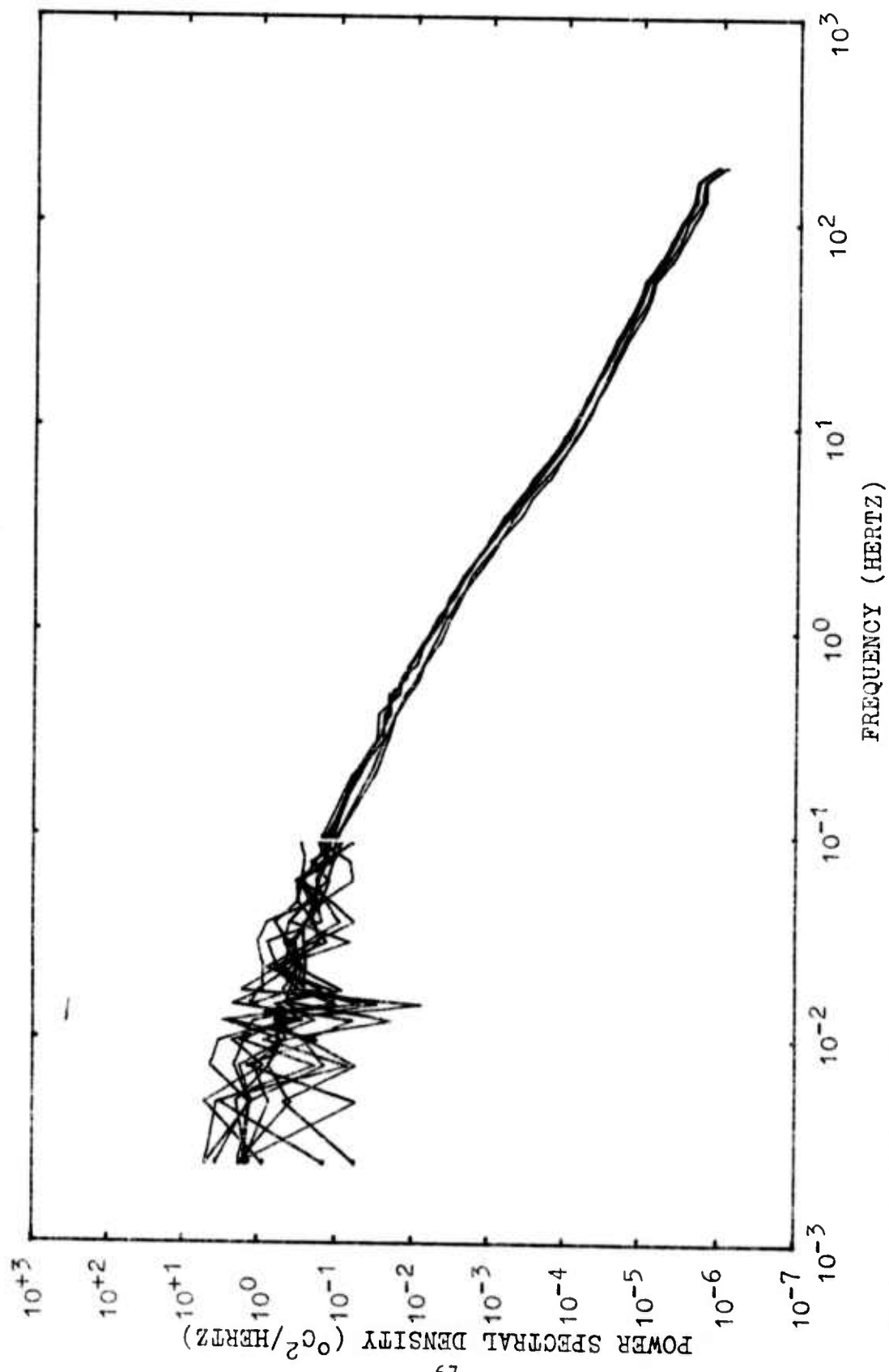


Fig. 5.6a. The combined set of high and low frequency experimental microtemperature spectra measured on May 25, 1972.

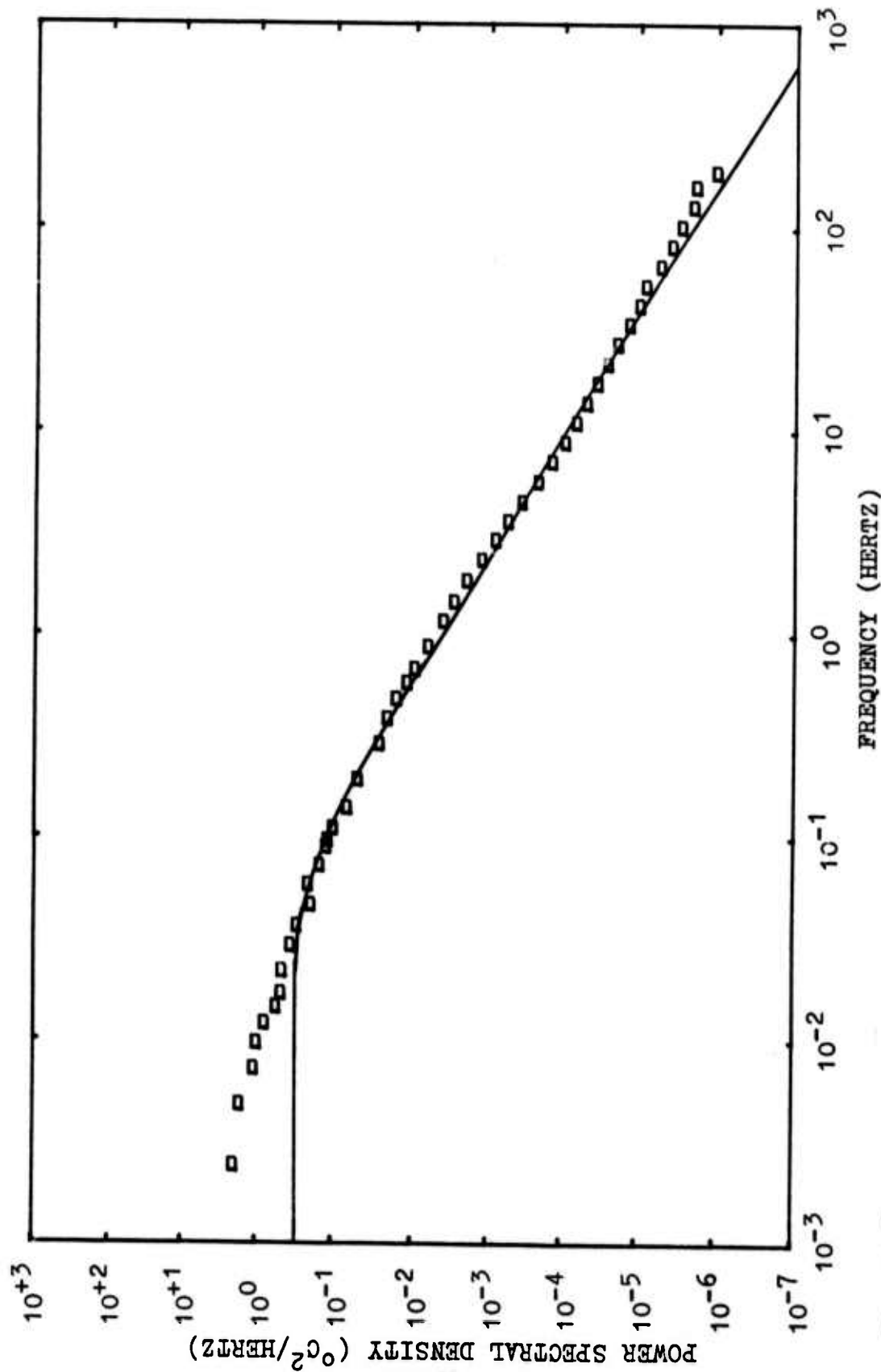


Fig. 5.6b. The mean experimental microtemperature spectrum (O) averaged over all the individual spectra of Fig. 5.6a. Theoretical curve based on von Karman's spectrum, using  $v=5.5$  m/s and  $L_0=2$  m.

## Chapter 6

### CONCLUSION

A series of experiments to measure the temporal power spectral density of the optical phase coherence perturbations across a laser wavefront due to atmospheric effects was conducted. The basic principles and equations of the underlying theory were presented and a theoretical phase difference power spectrum possessing a flat low frequency asymptote has been introduced. The measurement techniques and the data processing and analysis procedures were described. At the present time data from the first series of experimental measurements has been analyzed and data representing two typical conditions was presented.

Major emphasis was placed on analysis of averaged spectra to obtain adequate agreement with theoretical predictions of the spectral characteristics. Since the confidence limits of the resultant averaged spectra were dependent upon the number of spectral values averaged together, it was necessary to use lengthy data recording intervals to produce accurate spectral curves at the low frequencies of interest. For example, to produce spectral values at  $2.44 \times 10^{-3}$  hertz with ten degrees of freedom it was necessary to record ten, 6.8 minute data records or a total of 68 minutes of data. To maintain the stationarity of the characteristics of this atmospheric turbulence generated phenomenon it was therefore necessary to avoid gross changes in meteorological conditions over time periods of several hours. This

restricted the measurements to days of fairly constant meteorological conditions and prohibited data recording on days of changing weather fronts and systems. This problem indicates the difficulty experienced in measuring stationary, well-behaved spectra representative of the Kolmogorov and von Karman turbulence models.

The spectra from theoretical models consistently agreed with experimental data at higher frequencies where  $f > \sqrt{6} v_{\perp} / 2\pi\rho$ . This consistent agreement of the shape of theoretical and experimental spectra at high frequencies suggests that spectral values at these frequencies could be used to measure the refractive index structure function,  $C_n^2$ , from the high frequency asymptotic equation

$$C_n^2 \approx \left[ \left\{ \frac{1}{2} \right\} (.033) k^2 L (2\pi\rho)^{2/3} v_{\perp}^{-1} \right]^{-1} X^{+2/3} W(f). \quad (6-1)$$

The resulting value of  $C_n^2$  represents the integrated effect of the random variations in the refractive index field along the entire propagation path.

At medium and low frequencies the experimental and theoretical spectra were not always in agreement. The error between the curves at these frequencies was particularly sensitive to the wind speed and direction conditions. For low wind speeds and large wind direction variances the low frequency region of the spectrum failed to flatten out as theoretically predicted but instead continued to rise as frequency decreased. For moderate wind speeds and small wind direction variances the experimental and theoretical curves showed fair agreement as low as the low-frequency breakpoint at  $f = Av_{\perp} / 2\pi L_0$ .

In the low-frequency region below this frequency the power spectral curves were in error by an order of magnitude, the theoretical values being less than the experimental ones.

The excess power in the low frequencies of the phase-difference spectra as compared with theory (Figures 5.3 and 5.6) was traceable to excess power in those same frequencies in the microthermal spectra (Figures 5.3b and 5.6b). Since temperature variations almost entirely govern refractive index fluctuations for optical and infrared wavelengths, we determined that the theoretical basis for the phase-difference spectrum was not adequate. That basis is the commonly-used von Karman spectrum described by Reinhardt and Collins<sup>(3)</sup>. A new model which has more low frequency power and which better matches the microthermal spectra is the subject of a separate report by Greenwood and Taravano<sup>(10)</sup>.

## APPENDIX A

### Calculation of the Experimental Interference Pattern

The section of the Perkin Elmer analyzer which forms the phase interference pattern is shown schematically in Fig. A.1. In this diagram the secondary Dall-Kirkham, a reflective imager or condenser, is replaced by its optical equivalent, a converging lens of identical focal length and relative aperture number. The energy illuminating the sampling apertures is considered to be phase coherent across each individual aperture with a time-varying phase difference,  $\phi(t)$ , existing between the illumination at the two apertures.

To calculate the image plane intensity distribution it is necessary to calculate separately the image plane amplitude distribution due to the field illuminating each aperture, add the two resulting complex image plane amplitude distributions, and then compute the resultant image plane intensity distribution by finding the modulus squared of the sum of the complex amplitude distributions. These calculations will now be performed to yield the image plane intensity distribution  $I(x,y)$ .

The image plane amplitude distribution due to the illumination of aperture one by the field  $D_1 e^{is_1}$  is

$$E_1(x,y) = \iint D_1 e^{is_1} e^{-ikf^{-1}(x\xi+yn)} d\xi dn \quad (A-1)$$

where  $x$  and  $y$  are the image plane rectangular coordinates

$$k = 2\pi/\lambda$$

$\lambda$  = optical wavelength

$f$  = focal length of the convergent lens.

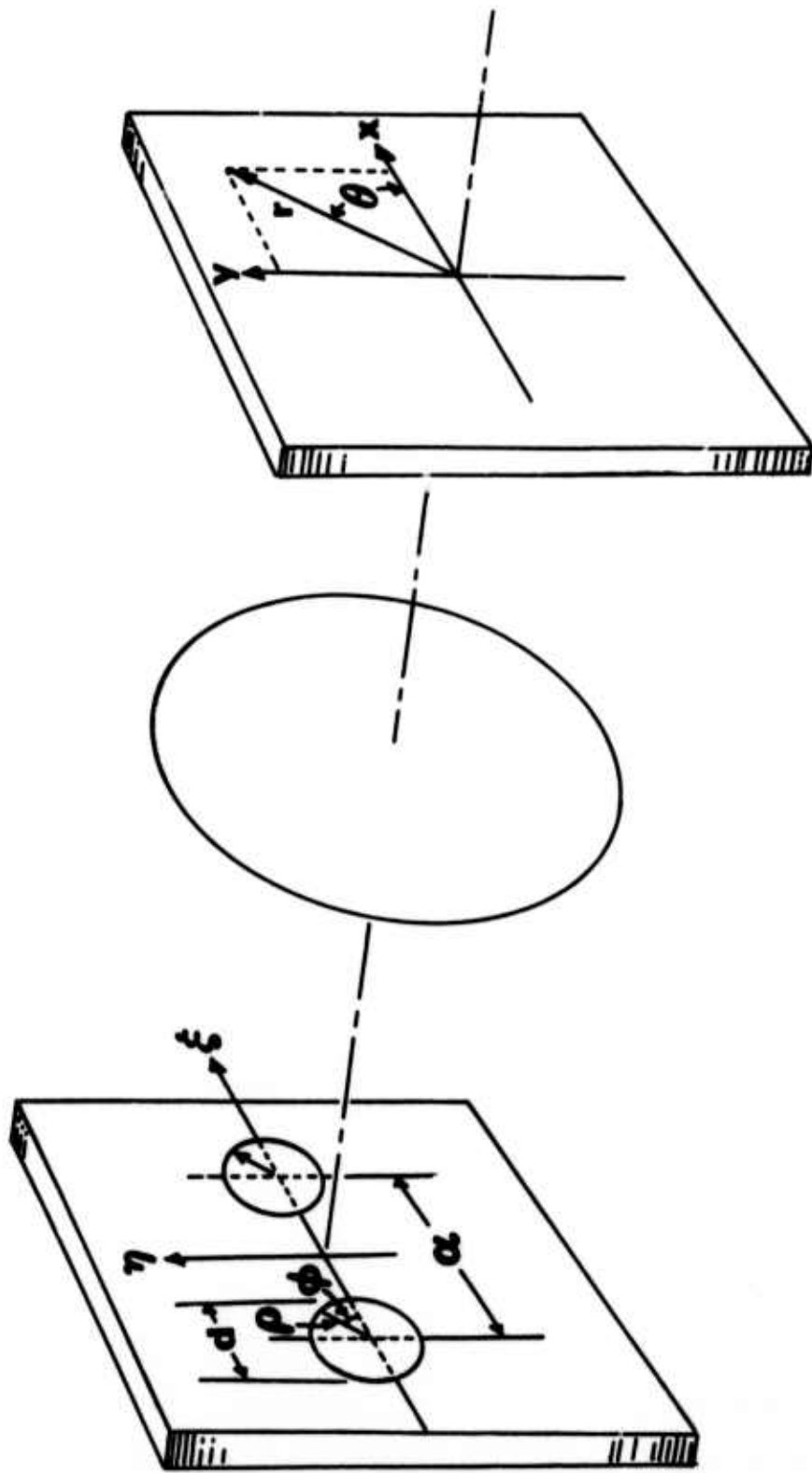


Fig. A.1. Illustration of a typical twin-aperture interferometer utilizing refractive optics.

The limits of integration extend over aperture one for (A-1).

Changing to the primed rectangular coordinate system ( $\xi'$  and  $n'$ ), whose origin lies at the center of aperture one and integrating over aperture one transforms (A-1) into the form

$$E_1(x,y) = e^{-ikx\alpha/2f} \iint_{D_1} e^{is_1} e^{-ikf^{-1}(x\xi'+yn')} d\xi' dn' \quad (A-2)$$

where  $\alpha$  = the separation of the 2 apertures

$$\xi' = \xi + \alpha/2$$

$$n' = n.$$

Converting to cylindrical coordinate systems in both the aperture and image planes changes (A-2) to

$$E_1(r,\theta) = e^{-\frac{ikr\alpha\cos(\theta)}{2f}} \int_{\rho=0}^{d/2} \int_{\phi=0}^{2\pi} D_1 e^{is_1} e^{-ikf^{-1}rp[\cos(\theta)\cos(\phi) + \sin(\theta)\sin(\phi)]} \rho d\rho d\phi \quad (A-3)$$

where  $r$  and  $\theta$  are the image plane cylindrical coordinates whose origin is on the optical axis

$\rho$  and  $\phi$  are the aperture plane cylindrical coordinates whose origin is at the center of aperture 1

$$\xi' = \rho \cos\phi$$

$$n' = \rho \sin\phi$$

$$x = r \cos\theta$$

$$y = r \sin\theta$$

$$d = \text{diameter of apertures one and two.}$$

By assuming that  $D_1$  and  $s_1$ , the amplitude and phase of the incident wave, are independent of  $\rho$  and  $\phi$ , (A-3) can be simplified to

$$E_1(r,\theta) = D_1 e^{is_1} e^{-\frac{ikr\alpha\cos(\theta)}{2f}} \int_{\rho=0}^{d/2} \int_{\gamma=0}^{2\pi} e^{-ikr\rho f^{-1}\cos(\gamma)} \rho d\rho d\gamma \quad (A-4)$$

for  $\gamma = \theta - \phi$ .

The integration over the range of  $\gamma$  may be performed by use of the identity

$$2\pi J_n(z) = i^{-n} \int_0^{2\pi} e^{iz \cos(\gamma)} e^{in\gamma} d\gamma \quad (\text{A-5})$$

to yield

$$E_1(r, \theta) = 2\pi D_1 e^{i(s_1 - \frac{kr\alpha \cos(\theta)}{2f})} \int_{\rho=0}^{d/2} \rho J_0(k\rho f^{-1}) d\rho \quad (\text{A-6})$$

The identity  $\int_0^b a J_0(a) da = b J_1(b)$  permits evaluation of the integral in (A-5) as

$$E_1(r, \theta) = 2\pi D_1 e^{i(s_1 - \frac{kr\alpha \cos(\theta)}{2f})} \left(\frac{d}{2}\right)^2 \left[ \frac{J_1(krd/2f)}{(krd/2f)} \right] \quad (\text{A-7})$$

which can be written as

$$E_1(x, y) = \pi D_1 e^{i(s_1 - \frac{k\alpha x}{2f})} \left(\frac{d}{2}\right)^2 \left[ \frac{2J_1(krd/2f)}{(krd/2f)} \right] \quad (\text{A-8})$$

where  $r = (x^2 + y^2)^{1/2}$ .

For  $K_1 = kd/2f$  and  $K_2 = k\alpha/f$  the image plane amplitude distribution due to the illumination only at aperture one is

$$E_1(x, y) = \pi D_1 e^{i(s_1 - \frac{K_2 x}{2})} \left(\frac{d}{2}\right)^2 \left[ \frac{2J_1(K_1 [x^2 + y^2]^{1/2})}{(K_1 [x^2 + y^2]^{1/2})} \right]. \quad (\text{A-9})$$

For  $E_2(x, y)$ , the image plane amplitude distribution due to the illumination at only aperture two, a similar derivation is possible, the only exception being that the quantity  $\xi'$  is defined as  $\xi' = \xi - \alpha/2$ .

The result is a sign change in the argument of the complex exponential phase term yielding

$$E_2(x, y) = \pi D_2 e^{i(s_2 + \frac{K_2 x}{2})} \left(\frac{d}{2}\right)^2 \left[ \frac{2J_1(K_1 [x^2 + y^2]^{1/2})}{(K_1 [x^2 + y^2]^{1/2})} \right] \quad (\text{A-10})$$

The image plane intensity distribution which is defined as the modulus squared of the image plane amplitude distribution,  $(E_1 + E_2)$ , is

$$I(x,y) = [E_1(x,y) + E_2(x,y)] \cdot [E_1(x,y) + E_2(x,y)]^* \quad (\text{A-11})$$

or

$$I(x,y) = E_1 E_1^* + E_2 E_2^* + E_1 E_2^* + E_2 E_1^* \quad (\text{A-12})$$

where "\*" implies complex conjugate.

Separately evaluating the above terms and for simplicity assuming that  $D_1 = D_2$  we derive the final expression

$$I(x,y) = M \left[ \frac{2J_1(K_1[x^2+y^2]^{1/2})}{(K_1[x^2+y^2]^{1/2})} \right]^2 [1 + \cos \{K_2 x + (S_1 - S_2)\}] \quad (\text{A-13})$$

$$\text{where } M = 4\pi^2 D^2 \frac{d^4}{2}$$

For the arrangement used for this experiment the pertinent parameters

$$\text{were } \alpha = 0.0381 \text{ meters}$$

$$d = 0.00381 \text{ meters}$$

$$\lambda = 1.06 \times 10^{-5} \text{ meters}$$

$$f = 0.903 \text{ meters.}$$

Based on these parameters the half-width of the Airy function,  $[\{2J_1(K_1[x^2+y^2]^{1/2})\} / \{K_1[x^2+y^2]^{1/2}\}]^2$ , to its first zero is 3.12mm. The length of one complete period for the cosinusoidal interference fringes is 0.254mm. Therefore, there are twelve complete cycles of the interference fringes within each half-width of the Airy function. Equation (A-13) also illustrates the important fact that the phase difference between the apertures,  $\phi(t) = S_1(t) - S_2(t)$ , phase modulates the spatial position of the cosinusoidal interference fringes in the x-direction of the image plane. An optical phase difference

of  $2\pi$  radians corresponds to a .254mm or one fringe period displacement of the interference fringes in the x-direction.

## APPENDIX B

### Reticle Error Analysis

This analysis concerns the error in the measurement of the position of the cosinusoidal interference fringes within the central lobe of the aperture diffraction pattern. This error arises from the use of a circular chopping reticle such as described in chapter 3 instead of an infinite series of parallel square waves of spatial frequency  $K_2$  matching the spatial frequency of the interference fringes.

For this analysis the assumption is made that the center of the interference pattern is located at the proper radial distance from the center of the reticle such that the arc length of the first radial wedge measured at that radius is equal to one period of spatial frequency  $K_2 = k\alpha/f$

where  $k = 2\pi/\lambda$

$\lambda$  = optical wavelength of the illumination

$\alpha$  = separation of interferometer apertures

$f$  = focal length of a converging lens used to form the interference pattern.

For the  $i$ -th wedge or cycle there are two errors; an error in the determination of the absolute location or position of that cycle denoted as  $E_{1,i}$ , and an error in the measurement of the length of the  $i$ -th interval denoted as  $E_{2,i}$ .

The positional error for each cycle of the reticle is greatest at that end of the cycle farthest from the center of the interference pattern. The calculation of the positional error will be performed for this point to yield the worst case positional error per cycle. The positional error will be expressed in percent of the ideal length of one cycle according to the formula

$$E_{1,i} = \{[S_i - H_i]/S_i\} \times 100 \quad (B-1)$$

where  $S_i$  = arc length to farthest edge of  $i$ -th cycle from interference pattern center which by definition is the ideal location of the  $i$ -th cycle

$H_i$  = height at which the radial line along farthest edge of  $i$ -th cycle intersects the vertical axis

$S_1$  = ideal length of one cycle for spatial frequency  $K_2$  and also the arc length of the first cycle.

From the geometry of the problem the quantity  $H_i$  may be expressed as  $H_i = r \tan(\theta_i)$  which by use of the arc length relationship,  $S_i = r\theta_i$ , becomes

$$H_i = \frac{S_i}{\theta_i} \tan(\theta_i). \quad (B-2)$$

The quantity  $r$  is the radial distance from the center of the reticle to the center of the interference pattern. The quantity  $\theta_i$  is the plane angle on the face of the reticle and is defined as the angle separating the radial line to the center of the interference pattern and the radial line to the far side of the  $i$ -th cycle.

Substituting (B-2) into (B-1) gives the following expression for the positional error

$$E_{1,i} = \{[S_i - [S_i/\theta_i] \tan(\theta_i)]/S_i\} \times 100. \quad (B-3)$$

The arc length of each interval or cycle of the reticle is equal, therefore,

$$S_i = i S_1. \quad (B-4)$$

Equation (B-3) can now be simplified to the form

$$E_{1,i} = \{i[1 - \{[\tan(i\theta_1)]/[i\theta_1]\}]\} \times 100. \quad (B-5)$$

The interval length error is computed as a percentage of the ideal interval length according to the formula

$$E_{2,i} = \{[S_i - [H_i - H_{i-1}]]/S_i\} \times 100. \quad (B-6)$$

Equation (B-2) can be used to reduce (B-5) to

$$E_{2,i} = \{1 - \{[S_i \tan(\theta_i)]/[S_i \theta_i]\} + \{[S_{i-1} \tan(\theta_{i-1})]/[S_{i-1} \theta_{i-1}]\}\} \times 100. \quad (B-7)$$

Substitution of (B-4) into (B-7) gives the equation for the interval length error as

$$E_{2,i} = \{1 - \{[\tan(i\theta_1)]/[\theta_1]\} + \{[\tan((i-1)\theta_1)]/[\theta_1]\}\} \times 100. \quad (B-8)$$

For the particular case of this experiment the reflective reticle consists of 940 complete cycles of spatial frequency  $K_2$ . Each cycle consists of a one-half period length reflecting surface and a one-half period absorbing surface. The quantity  $\theta_1$  is equal to  $2\pi/940$  or 0.00668424 radians. Initial attempts to calculate the errors by use of the power series approximation for the tangent of angle  $\theta_1$  showed the necessity to include the fifth power of the angle. Subsequently a short computer program was written to calculate both errors by use of the computer's tangent function. Table B.1 contains a tabulation of both errors for the first twenty-five reticle cycles.

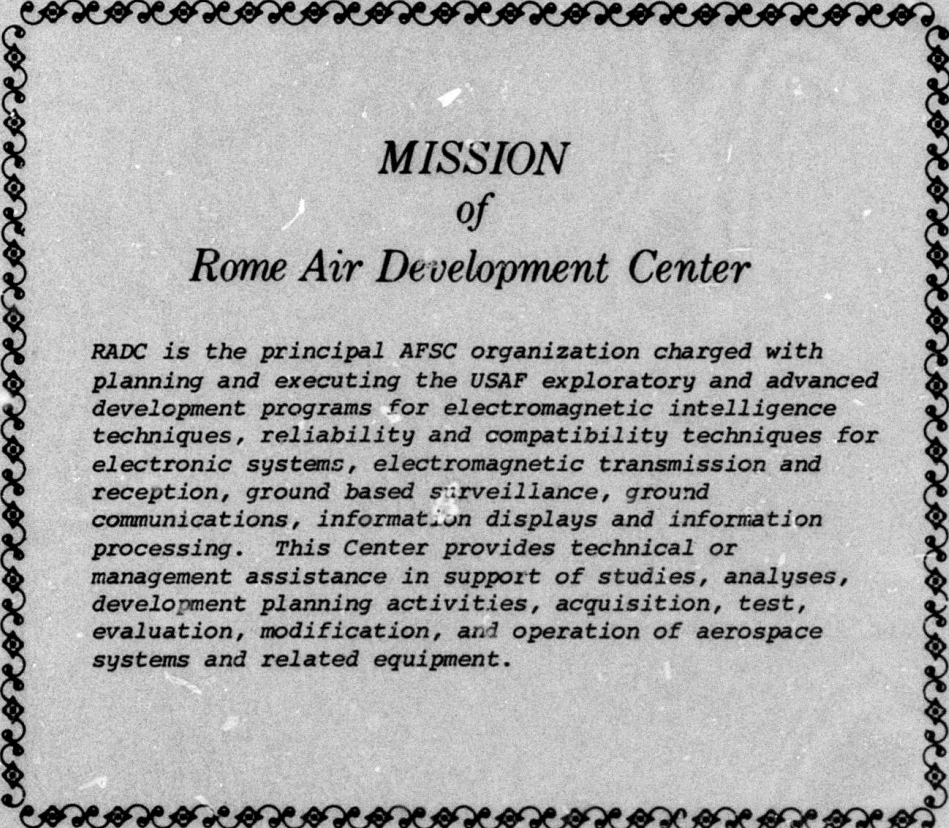
Table B.1  
Error Due to Circular Reticle

Interference Fringe Number	Percent Positional Error	Percent Interval Length Error
1	$1.489 \times 10^{-3}$	$1.489 \times 10^{-3}$
2	$1.192 \times 10^{-2}$	$1.043 \times 10^{-2}$
3	$4.022 \times 10^{-2}$	$2.83 \times 10^{-2}$
4	$9.53 \times 10^{-2}$	$5.51 \times 10^{-2}$
5	$1.86 \times 10^{-1}$	$9.09 \times 10^{-2}$
6	$3.22 \times 10^{-1}$	$1.36 \times 10^{-1}$
7	$5.11 \times 10^{-1}$	$1.89 \times 10^{-1}$
8	$7.63 \times 10^{-1}$	$2.52 \times 10^{-1}$
9	1.09	$3.24 \times 10^{-1}$
10	1.49	$4.05 \times 10^{-1}$
11	1.99	$4.95 \times 10^{-1}$
12	2.58	$5.94 \times 10^{-1}$
13	3.28	$7.02 \times 10^{-1}$
14	4.10	$8.19 \times 10^{-1}$
15	5.05	$9.46 \times 10^{-1}$
16	6.13	1.08
17	7.35	1.23
18	8.74	1.38
19	$1.03 \times 10^1$	1.55
20	$1.20 \times 10^1$	1.72
21	$1.39 \times 10^1$	1.90
22	$1.60 \times 10^1$	2.09
23	$1.83 \times 10^1$	2.30
24	$2.08 \times 10^1$	2.51
25	$2.35 \times 10^1$	2.73

Table B.1 shows that, except for the first cycle where both errors are equal and are  $1.489 \times 10^{-3}$  percent, the positional error is greater than the interval length error. As explained in the body of the text, the highest order fringe or cycle to effect the experimental measurement is the seventh cycle. For the seventh cycle the positional error is 0.5113 percent and the interval length error is 0.1894 percent to give a worst case error of 0.7007 percent of one interval.

## REFERENCES

1. V. I. Tatarski, The Effects of the Turbulent Atmosphere on Wave Propagation, NTIS-IT No. 68-50464, Edited by J. W. Strobehn (National Technical Information Service, Springfield, Va., 1971) Ch. 4.
2. S. F. Clifford, "Temporal-Frequency Spectra for a Spherical Wave Propagating Through Atmospheric Turbulence", Journal of the Optical Society of America, Vol. 61, No. 10, pp 1285-1292, October 1971.
3. G. W. Reinhardt and S. A. Collins, Jr., "Outer-scale Effects in Turbulence-Degraded Light-Beam Spectra", Journal of the Optical Society of America, Vol. 62, No. 12, pp 1526-1528, December 1972.
4. D. P. Greenwood, Rome Air Development Center, Environmental Studies Section, Rome, New York, private communication, October 1972.
5. J. L. Lumley and H. A. Panofsky, The Structure of Atmospheric Turbulence, New York: Interscience, 1964, Ch. 4.
6. J. C. Wyngaard, Air Force Cambridge Research Laboratories, Boundary Layer Branch, Hanscom Field, private communication, October 1972.
7. A. V. Oppenheim and C. J. Weinstein, "Effects of Finite Register Length in Digital Filtering and the Fast Fourier Transform", Proceedings of the IEEE, Vol. 60, No. 8, pp 957-976, August 1972.
8. M. Abramowitz and I. A. Stegun, Handbook of Mathematical Functions, Washington: U.S. Government Printing Office, 1964; New York: Dover, 1965.
9. G. R. Ochs, A Resistance Thermometer for Measurement of Rapid Air Temperature Fluctuations, ESSA Technical Report IER 47-ITSA 46 (U.S. Dept of Commerce, Washington DC, October 1967).
10. D. P. Greenwood and D. O. Tarazano, A Proposed Form for the the Atmospheric Microtemperature Spatial Spectrum in the Input Range, RADC Technical Report, RADC-TR-74-19, February 1974.

A decorative border with a repeating scrollwork pattern surrounds the central text.

*MISSION*  
*of*  
*Rome Air Development Center*

*RADC is the principal AFSC organization charged with planning and executing the USAF exploratory and advanced development programs for electromagnetic intelligence techniques, reliability and compatibility techniques for electronic systems, electromagnetic transmission and reception, ground based surveillance, ground communications, information displays and information processing. This Center provides technical or management assistance in support of studies, analyses, development planning activities, acquisition, test, evaluation, modification, and operation of aerospace systems and related equipment.*